Combined Photoacoustic and Doppler Ultrasound Imaging for Tissue Oxygen Consumption Estimation

by

Yan Jiang

A thesis submitted in partial fulfillment of the requirements for the degree of

Doctor of Philosophy

in

Biomedical Engineering

Department of Electrical and Computer Engineering
University of Alberta

© Yan Jiang, 2019

Abstract

Oxygen is the substrate that cells use in the greatest quantity and upon which aerobic metabolism and cell integrity depend. Continuous and sufficient supply of oxygen is necessary to maintain normal cellular aerobic metabolism. Failure of oxygen supply to meet metabolic needs is a common feature of many tissue dysfunctions and diseases. Therefore, the ability to estimate metabolic rate of tissue oxygen consumption (MRO_2) is important for diagnosis and therapy of many diseases related to metabolism functions.

Currently, techniques to obtain MRO_2 are limited. None of the single modalities has good performance both at blood flow and oxygenation measurements. Therefore, the long-term goal of our research is to develop a multi-modality imaging technique combining photoacoustic and Doppler ultrasound methods for non-invasive MRO_2 estimation *in vivo* in animal and human subjects. Photoacoustic imaging provides high spatial resolution and high sensitivity in blood oxygenation estimation due to high physiologically specific optical absorption contrast. Doppler ultrasound is capable of imaging a wide range of flow velocities by choosing appropriate ultrasonic transducer and Doppler pulse-repetition-rate. The combination of these two imaging modalities has the potential to better visualize and estimate MRO_2 for many research and clinical applications.

In this dissertation, we propose MRO_2 estimation using combined multi-wavelength photoacoustic microscopy and high-frequency (>20MHz) Doppler ultrasound. We aim to devise flow phantom experiments to validate the capabilities of our technique for MRO_2 estimation, and further demonstrate the feasibility of cerebral MRO_2 estimation in brain auto-regulation study *in vivo* in a pre-clinical animal model. Work conducted in this dissertation can be described in three sections. First, we developed a combined photoacoustic and high-frequency power Doppler ultrasound

imaging system for blood volume detection, which is important for flow estimation. We presented a quantitative and objective comparison on blood volume detection using flow phantoms with various combinations of vessel size, flow velocity and optical wavelength. Second, we upgraded our system to introduce blood oxygen saturation estimation using multi-wavelength photoacoustic method, and color Doppler ultrasound for flow velocity estimation. We experimentally demonstrated the feasibility to image local blood oxygen flux of a single vessel by double-ink phantom studies, and *in vitro* sheep blood phantom studies. Third, we pushed forward our research to pre-clinical domain, and first demonstrated the cerebral MRO_2 estimation *in vivo* by combining the measurements of arterial and venous oxygen saturation, and flow rate of internal jugular vein on a Sprague Dawley rat model. In this study, the physiological conditions of the animal were controlled from hypoxia to mild hyperoxia, to study the hypothesis of brain metabolic auto-regulation mechanisms. This research may have significant applicability in other tissues and has the potential for clinical translation in the future.

Preface

- Chapter 3 of this thesis has been published as Y. Jiang, T. Harrison, J. C. Ranasinghesagara, R. J. Zemp, "Photoacoustic and high-frequency power Doppler ultrasound biomicroscopy: a comparative study," *Journal of Biomedical Optics,* vol. 15, no. 5, p. 056008, 2010. I was responsible for the experiment design and implementation, signal processing, data collection and analysis, manuscript composition, and also participated in the system development. T. Harrison and J. C. Ranasinghesagara contributed to system development. R. J. Zemp was the supervisory author and was involved with concept formation and manuscript composition. The full copyright notice and citation can be found:

  Y. Jiang, T. Harrison, J. C. Ranasinghesagara, R. J. Zemp, "Photoacoustic and high-frequency power Doppler ultrasound biomicroscopy: a comparative study," *Journal of Biomedical Optics*, vol. 15, no. 15, p. 056008, 2010.

  DOI: https://doi.org/10.1117/1.3491126.

- Chapter 4 of this thesis has been published as Y. Jiang, A. Forbrich, T. Harrison, R. J. Zemp, "Blood oxygen flux estimation with a combined photoacoustic and high-frequency ultrasound microscopy system: a phantom study," *Journal of Biomedical Optics,* vol. 17, no. 3, p. 036012, 2012. I was responsible for the system development, experiment design and implementation, signal processing, data collection and analysis, manuscript composition, and also participated

in the system development. A. Forbrich and T. Harrison contributed to the system development. R. J. Zemp was the supervisory author and was involved with concept formation and manuscript composition. The full copyright and citation can be found:

- Chapter 5 of this thesis has been published as Y. Jiang, R. J. Zemp, "Estimation of cerebral metabolic rate of oxygen consumption using combined multi-wavelength photoacoustic microscopy and Doppler micro-ultrasound", *Journal of Biomedical Optics*, vol. 23, no. 1, p. 016009, 2018. I was responsible for the system development, experiment design and implementation, signal processing, data collection and analysis and manuscript composition. R. J. Zemp was the supervisory author and was involved with concept formation and manuscript composition. The full copyright and citation can be found:

- *In vivo* experiments procedures involving animals described in Chapter 5 in this thesis followed the laboratory animal protocol approved by University of Alberta Animal Use and Care Committee.

Acknowledgements

First and most of all, I would like to thank my supervisor, Dr. Roger J. Zemp, for his expertise, guidance, and support throughout my doctoral program. Thanks for his patience, understanding and encouragement to help me get through hard times and complete my thesis, and his dedication in teaching and mentorship to help me well prepared for the future career. It was a great pleasure to work with him, and there were so many good memories during my stay in University of Alberta.

Then I would like to acknowledge my co-authors: Alex Forbrich, Tyler Harrison, and J. C. Ranasinghesagara for their great help and insights on publications, and my thesis committee: Dr. Dileepan Joseph, Dr. Mrinal Mandal, Dr. Manisha Gupta, and Dr. Shuo Tang for their valuable comments and kind encouragement. I also appreciate the help and support from all my teachers and colleagues in the Department of Electrical and Computer Engineering.

Last of all, I would like to thank my family, especially my parents, my husband and my son little Christopher. This accomplishment would not have been possible without their unconditional love and continuous encouragement and support.

Contents

List of Tables

List of Figures

Fig.5.6 The estimated representative $CMRO_2$ (ml/100g/min) as a function of varying global arterial sO_2 measured using pulse oximetry during modulation of FiO_2 under anesthesia. Error bars are standard deviations estimated according to the theory of propagation of errors.

List of Abbreviations

MRO_2: Metabolic Rate of Oxygen Consumption

$CMRO_2$: Cerebral Metabolic Rate of Oxygen Consumption

CBF: Cerebral Blood Flow

C_{THb}: Total Concentration of Hemoglobin

HbO_2: Oxy-Hemoglobin

Hb: Deoxy-Hemoglobin

sO_2: Blood Oxygen Saturation

PAM: Photoacoustic Microscopy

pO_2: Partial Pressure of Oxygen

ROC: Receiver Operating Characteristic

TPF: True Positive Fraction

FPF: False Positive Fraction

ROI: Region of Interest

SNR: Signal to Noise Ratio

PRF: Pulse Repetition Frequency

RF: Radio Frequency

DKLT: Discrete Karhunen-Loeve Transform

CW: Continuous Wave

PW: Pulsed Wave

PET: Positron Emission Tomography

MRI: Magnetic Resonance Imaging

1. Introduction

1.1. Tissue Metabolic Oxygen Consumption

In order for cells to remain viable and to perform their genetically programmed functions they must produce usable energy. This energy is commonly stored in adenosine triphosphate (ATP) and released during the hydrolysis of the terminal phosphate bond. In cells with functional mitochondria, approximately 88% of ATP molecules (about 28/32 of total ATP molecules) are produced by oxidative metabolism of glucose [2]. The metabolic rate of oxygen consumption (MRO_2) is an important indicator of tissue viability and functionality.

In normal tissues the oxygen supply meets the requirements of the cells. This is accomplished by modulating tissue blood flow and/or by changing the oxygen extraction in accordance with alterations in physiological conditions [3]. In poorly perfused tumors, modulations of both mechanisms are rather limited due to rapid proliferations of tumor cells. Oxygen deficiency (hypoxia) is a common feature in malignancies [3], and the presence of a large number of hypoxic regions within a tumor usually correlates with a poor prognosis [2]. This metabolic phenotype has been investigated for tumor imaging, for example, by positron emission tomography (PET) to improve the diagnosis and subsequent treatment of cancers [4].

The brain is one of the most energy-demanding and metabolically active organs of the body. Although it comprises only 2% of the body weight, it receives about 15% of cardiac output and uses 20% of total body oxygen [5]. This highlights the critical dependence of brain function on continuous, efficient usage of oxygen, and the organ's heightened sensitivity to alterations in oxygen supply. Many of the common disorders of the brain, such as Alzheimer's [6], Parkinson's [7], Huntington's [8], and others have been found to be associated with alterations in the cerebral oxygen metabolism. In addition, a measure for assessing the cerebral MRO_2 will further enhance our understanding of normal cerebral physiology during rest, sleep [9], anesthesia [10], aging [11], and functional brain tasks, as well as be useful for the monitoring and management of patients who are at the risk of developing brain hypoxia-ischemia [12].

Moreover, there are other diseases and pathophysiological functions closely related to alterations in tissue oxygen metabolism: examples include diabetes [13], burns [14], stroke [15], congestive heart failures [16], etc. Thus, a robust and reliable measure for quantifying MRO_2 would serve as

an important tool for diagnosis and therapy of many diseases as well as for metabolism related pathophysiological studies.

1.2. Problem and Motivation

MRO_2 is defined as the amount of oxygen consumed in a given tissue region per unit time per 100g of tissue or the organ of interest [17]. Blood flow and oxygen extraction of the defined tissue region are the key parameters to estimate MRO_2. Important criteria for a useful MRO_2 imaging technique include noninvasiveness, adequate spatial and temporal resolution, ability to quantify oxygenation levels, low radiation exposure, good safety profile, and widespread clinical availability [18]. Unfortunately, no *in vivo* method can fulfill all of these requirements. Currently, techniques to obtain MRO_2 are limited. In early studies, the jugular vein oximetry involving catheterization has been used for a surrogate measure of cerebral MRO_2 but is invasive [19]. PET is widely used for imaging MRO_2 in clinical practice [20]. However, the spatial resolution is poor (~1cm for clinical system), and the injection or inhalation of radioactively labeled exogenous tracers results in a complex procedure with exposure to ionizing radiation, which prevents its frequent use on the same patient. Functional Magnetic Resonance Imaging (MRI) has also been widely used to image MRO_2 especially for the brain. MRI is noninvasive and can be performed with high spatial resolution, but it is only sensitive to deoxy-hemoglobin and has trouble distinguishing between changes in oxygen saturation and blood flow [21]. Moreover, the complex setup and high expenses preclude PET and MRI for many bedside clinical applications.

Imaging techniques based on optical contrast, which is sensitive to blood functional parameters, have been widely employed for the assessment of tissue oxygen metabolism. Near-Infrared Spectroscopy (NIRS) offers a means to estimate MRO_2 noninvasively, but it relies on an approximate theoretical model or other techniques to estimate blood flow (such as Doppler ultrasound) [22] . Recently diffuse correlation spectroscopy (DCS) has been combined to provide flow information [23]. The main drawback is that the spatial resolution is relatively low due to strong optical scattering. Photoacoustic imaging overcomes this limitation by ultrasonically imaging optical contrast through the photoacoustic effect [17]. Optical-resolution photoacoustic microscopy (OR-PAM) has been used to estimate oxygen consumption in superficial tissues [24]. This technique utilizes fine optical focusing to achieve high lateral resolution (~5µm), however, the imaging depth is shallow (<1mm) and the detectable flow speed (<12mm/s) is limited due to

low laser repetition rate [25]. While recent work suggests hope for photoacoustic flow estimation in deep tissues (>1mm) using acoustic-resolution photoacoustic imaging [26], it is less established than Doppler ultrasound methods we selected in this study.

1.3. Long-term goal and proposed research

The long-term goal of our research is to develop a multi-modality imaging technique combining photoacoustic and Doppler ultrasound methods for non-invasive MRO_2 estimation *in vivo* in animal and human subjects. Photoacoustic imaging provides better spatial resolution than NIRS by taking advantage of ultrasonic detection, and higher sensitivity than MRI (or PET) in blood oxygenation estimation due to high physiologically specific optical absorption contrast. Doppler ultrasound is capable of imaging a wide range of flow velocities at greater imaging depths (>1mm) than photoacoustic Doppler flowmetry by choosing appropriate ultrasonic transducer and Doppler pulse-repetition-rate. The combination of these two imaging modalities has the potential to better visualize and estimate MRO_2 for many research and clinical applications: for example, the study of brain auto-regulation mechanism under different physiological conditions, tumor hypoxia imaging for cancer diagnosis, and local ischemia monitoring, etc. Moreover, this proposed technique is completely non-invasive, requires no contrast agents and could be inexpensive enough to be used in many settings including research labs, pharmaceutical companies and medical clinics.

In this dissertation, we propose MRO_2 estimation using combined multi-wavelength photoacoustic microscopy and high-frequency Doppler ultrasound. High-frequency Doppler ultrasound (>20MHz) provides high spatial and velocity resolution, which is important for imaging small animal models. We aim to devise flow phantom experiments to validate the capabilities of our technique for MRO_2 estimation, and further demonstrate the feasibility of cerebral MRO_2 estimation in brain auto-regulation study *in vivo* in a pre-clinical animal model. This dissertation does not yet aim for human translation, but rather to demonstrate the key points of feasibility for clinical applications. Human translation may be possible in the future with infrared light and diagnostic-frequency (1-15MHz) transducers, especially in infants and children.

1.4. Major contribution of this dissertation

Work conducted in this dissertation can be described in three sections.

1.4.1. Comparative study on blood volume detection

- We pioneered to develop a combined photoacoustic and high-frequency power Doppler ultrasound imaging system for the first time. This system uses a swept-scan 25MHz ultrasound transducer with confocal dark field laser illumination optics. A pulse-sequencer enables laser and Doppler pulses to be interleaved so that photoacoustic and power Doppler images can be co-registered. Signal processing strategies include a correlation-based signal alignment algorithm for swept-scan, wall-filtering and Doppler power calculations.

- Blood volume detection is important for flow estimation when quantifying MRO_2. While many groups have demonstrated the capability of imaging blood volume fraction using photoacoustic imaging or power Doppler ultrasound separately, no one combines and compares them in such a study. By using our combined imaging system, we presented a quantitative and objective comparison on blood volume detection using flow phantoms with various combinations of vessel size, flow velocity, and optical wavelength. This study highlights relative merits and shortcomings of these two imaging modalities, gives further guidance on fractional blood volume estimations *in vivo* under complicated circumstances.

1.4.2. Phantom validation on blood oxygen flux estimation

- We upgraded our previous system in Section 1.4.1 to introduce blood oxygen saturation estimation using multi-wavelength photoacoustic method and flow velocity estimation using color Doppler ultrasound. A tunable optical parametric oscillator is pumped by a Q-switch Nd:YAG laser to provide a tuning range of 410nm to 710nm. Color Doppler velocity estimation is based on an auto-correlation algorithm first proposed by Kasai et al [27].

- We experimentally demonstrated for the first time the feasibility to image local blood oxygen flux of a single vessel using our combined photoacoustic and Doppler ultrasound imaging system, along with mean flow velocity measured by color Doppler ultrasound, vessel cross-sectional area measured by power Doppler or structural photoacoustic imaging, and oxygen saturation and total concentration of hemoglobin measured by multi-wavelength photoacoustic method.

- Double-ink phantom studies have been conducted to determine the accuracy of flow velocity and blood oxygen saturation (sO_2) estimation. Red and blue ink samples were diluted and mixed in various volumetric ratios to mimic different levels of sO_2. Then the double-ink blood mimicking fluid was pumped through corresponding vessels at different flow rates using a calibrated syringe pump. This is a good first step towards oxygen flux estimation because all the measurements can be easily validated.

- *In vitro* sheep blood phantom experiments have been performed to demonstrate the capability of imaging blood oxygen flux. Various sO_2 levels were obtained by mixing the freshly collected sheep blood with certain ratios of oxygen and carbon dioxide. Blood with various sO_2 levels were then pumped through corresponding vessels embedded in tissue-mimicking base at different flow rates. Blood oxygen flux was estimated from measurements of all the key parameters, and the uncertainty of the estimate was quantified. This work is important for our next step towards *in vivo* MRO_2 estimation.

1.4.3. Cerebral oxygen consumption estimation

- We first demonstrated and reported the cerebral MRO_2 estimation *in vivo* by combining the measurements of arterial and venous oxygen saturation, and flow rate of internal jugular vein on a Sprague Dawley rat model. Due to the complexity of *in vivo* measurements, we re-designed the optics of our imaging probe and deployed some new approaches for blood sO_2 and flow estimation.

- We adopted a Doppler bandwidth broadening technique to transverse flow estimation since *in vivo* measurements were to be done along vessels almost perpendicular to the ultrasound beam axis. Also, since it was significantly more challenging for sO_2 estimation *in vivo*, we implemented two independent photoacoustic methods for a cross-validation. The first approach is based on traditional multispectral unmixing. The second approach is to use multi-wavelength photoacoustic measurements at different sO_2 levels and solve a system of equations to estimate the different sO_2. Unlike the first approach, this second method requires no wavelength-dependent fluence calibration factor.

- Animal models experiments were performed with Sprague Dawley rats. The physiological conditions of the animal were controlled by varying the fraction of inspired oxygen. In this

study, mild hypoxia to mild hyperoxia (partial pressure of oxygen within the range of 30-100mmHg) was introduced to avoid significant changes in cerebral oxygen consumption. Estimates of cerebral MRO_2 under different physiological conditions were based on arterial and venous oxygen saturation measurements using photoacoustic methods, and flow measurements using Doppler bandwidth broadening. The results have shown that the cerebral MRO_2 remains relatively constant from mild hypoxia to mild hyperoxia, which agrees with the hypothesis of brain metabolic auto-regulation mechanism. This technique for estimating oxygen consumption may have significant applicability in other tissues and has potential for clinical translation owing to its label free nature.

1.5. Organization of this dissertation

The rest of the dissertation is organized as: Chapter 2 provides background information on principles of Doppler ultrasound and photoacoustic imaging, and the techniques we used in this dissertation for flow estimation and blood oxygen saturation estimation. Chapter 3 is focused on comparative study of blood volume detection, Chapter 4 is focused on the phantoms studies of blood oxygen flux estimation, and Chapter 5 is focused on *in vivo* cerebral oxygen consumption estimation. Chapter 6 is a summary of contributions, offers conclusions and discussions of future work.

Contents of this dissertation are drawn from the publications with permissions listed as following:

[1] Y. Jiang, R. J. Zemp, "Estimation of cerebral metabolic rate of oxygen consumption using combined multi-wavelength photoacoustic microscopy and Doppler micro-ultrasound," *Journal of Biomedical Optics*, vol. 23, no. 1, p. 016009, 2018.

[2] Y. Jiang, A. Forbrich, T. Harrison, R. J. Zemp, "Blood oxygen flux estimation with a combined photoacoustic and high-frequency ultrasound microscopy system: a phantom study," *Journal of Biomedical Optics*, vol. 17, no. 3, p. 036012, 2013.

[3] Y. Jiang, T. Harrison, A. Forbrich, R. J. Zemp, "*In vivo* combined photoacoustic and Doppler ultrasound imaging," in Proc. SPIE, vol. 8223, 822315, San Francisco, 2012.

[4] Y. Jiang, T. Harrison, A. Forbrich, R. J. Zemp, " "Oxygen consumption estimation with combined color Doppler ultrasound and photoacoustic microscopy: a phantom study," in Proc. SPIE, vol. 7899, 789942, San Francisco, 2011.

[5] Y. Jiang, T. Harrison, R. J. Zemp, "Photoacoustic and Doppler ultrasound for oxygen consumption estimation: implementation on a clinical array system," in Proc. SPIE, vol. 7899, 789941, San Francisco, 2011.

[6] Y. Jiang, T. Harrison, J. Ranasinghesagara, R. J. Zemp, "Photoacoustic and high-frequency power Doppler ultrasound biomicroscopy: a comparative study," *Journal of Biomedical Optics*, vol. 15, no. 5, p. 056008, 2010.

[7] Y. Jiang, T. Harrison, J. Ranasinghesagara, R. J. Zemp, "Combined photoacoustic and high-frequency power Doppler ultrasound imaging," in Proc. SPIE, vol. 7564, 756404, San Francisco, 2010.

2. Background and Literatures

2.1. Tissue Metabolic Oxygen Consumption

2.1.1. Metabolic rate of oxygen consumption (MRO$_2$)

Oxygen is the substrate that cells use in the greatest quantity and upon which aerobic metabolism and cell integrity depend. Since tissues have no storage system for oxygen, a continuous supply at a rate that matches changing metabolic requirements is necessary to maintain aerobic metabolism and normal cellular function. Failure of oxygen supply to meet metabolic needs is the feature common to many tissue dysfunction and diseases. In tumors, it has long been recognized that oxygen deficiency (hypoxia) usually indicates malignancies, and may influence the response of therapies including aggressiveness, local recurrence and overall prognosis [28]. In acute stroke, to better understand the metabolic state of the ischemic brain may improve the ability to identify the tissue at risk of infarction and help to select patients for reperfusion therapies [29]. In addition, many brain disorders, such as Alzheimer's disease [6] and Parkinson's disease [7], are found to be closely associated with alterations in cerebral oxygen metabolism. Therefore, an accurate measurement of tissue metabolic rate of oxygen consumption (MRO$_2$) would not only enable a better understanding of normal physiologies, but also be a powerful tool for research and clinical diagnosis and therapy of cancer and many other diseases related to metabolism functions.

In general, MRO$_2$ is defined as the amount of oxygen consumed in a given tissue region per unit time per 100g of tissue or the organ of interest [17]. If the region of interest is well defined, for N feeding vessels and M draining vessels, MRO$_2$ can be expressed as:

$$MRO_2 = [\textstyle\sum_i^N \Phi_{O_2}{}^{in}(i) - \sum_j^M \Phi_{O_2}{}^{out}(j)]/w, \qquad (2.1)$$

where Φ_{O_2} is the oxygen flux, defined as the volume of oxygen content transported per unit time in each single blood vessel, and w is the weight of the region of interest (in gram). Since the oxygen content in blood is the summed contribution of oxygen that is dissolved in plasma and chemically bound to hemoglobin in red blood cells, the oxygen flux in a single vessel can be expressed as:

$$\Phi_{O_2} = F \times (\zeta \times C_{Hb} \times sO_2 + \alpha_{O_2}(T) \times pO_2), \qquad (2.2)$$

where F is the blood flow rate, C_{Hb} is the total concentration of hemoglobin, sO_2 is the oxygen saturation of hemoglobin (defined as the fraction of hemoglobin which is oxygenated), and pO_2 is

the partial pressure of the oxygen dissolved in plasma. The constants ζ is the oxygen-binding capacity of hemoglobin (typically 1.34ml/g), and $\alpha_{O_2}(T)$ is the solubility coefficient of the oxygen dissolved in plasma dependent on temperature [30]. In different applications, the estimation is different. For example, since the solubility of oxygen is limited in plasma, the specialized oxygen-binding mechanism of hemoglobin is the major means of transporting oxygen in blood [30]. However, in the case of small capillaries, oxygen in plasma can diffuse through capillary walls and into cells for aerobic metabolism, thus it plays an important role for cells and should be estimated. As in Eq.(2.2), when the oxygen in plasma is negligible, blood flow and oxygen saturation of hemoglobin are the key parameters to estimate MRO_2.

2.1.2. Progress and challenges on MRO_2 estimation

For MRO_2 estimation, some important criteria for a useful imaging technique should be addressed, such as noninvasiveness, ability to quantify blood flow and oxygenation levels, adequate spatial and temporal resolution, adequate imaging depth, low radiation exposure, good safety profile, and widespread clinical availability [18]. Currently, three primary imaging modalities have been investigated and developed to quantify MRO_2. Among them, positron emission tomography (PET), a noninvasive imaging technique that detects gamma rays from positron-emitting isotopes, is most widely used in clinical practice [4]. The increased uptake of radiotracer 18F-fluorodeoxyglucose (FDG) due to increased glucose metabolism in most types of tumor cells, makes PET intrinsically suitable for tumor hypoxia imaging, as is the case in most lung, stomach, head and neck, cervical and breast cancers, as well as melanoma and lymphoma [31]. PET can also provide direct measurement of cerebral MRO_2 through imaging of the accumulated inhaled radioactive labeled oxygen ($^{15}O_2$) in the brain, which is converted into ^{15}O-labeled water after distribution into the tissue [32]. Some drawbacks of PET for MRO_2 estimation include the poor spatial resolution which is about 1cm in clinical systems, and the restrictive utility due to the high radiation dose, relatively complex setup required for the constant delivery of the inhalation or injection of the radiotracers, high expenses and long scanning time.

Functional magnetic resonance imaging (fMRI) has also been widely used to image MRO_2, especially in cognition studies and applications [33]. The well-known blood oxygen level dependent (BOLD) effect can detect changes in deoxyhemoglobin concentration consequent to task-induced or spontaneous modulation of neural metabolism [33]. In previous studies, BOLD-

fMRI has been used to noninvasively quantify cerebral MRO_2 based on the measurement of transverse relaxation time T2 with high spatial and temporal resolution [34]. However, since it is only sensitive to deoxyhemoglobin, this method relies on an *in vitro* calibration curve to translate T2 measurements to venous oxygen saturation and has trouble distinguishing between changes in oxygen saturation and blood flow. Recently, phase-contrast MRI has been proposed to quantify the blood flow in major inflow vessels, however, for the oxygen saturation estimation only large-sized vein (superior sagittal sinus) can be targeted [35]. Moreover, the complex setup and high expenses preclude MRI for many bedside clinical applications.

Optical imaging and spectroscopic methods offer a unique strategy for noninvasive and inexpensive MRO_2 estimation. One example is to use near-infrared spectroscopy (NIRS), which combines diffuse optical spectroscopy (DOS) to measure oxygen saturation of hemoglobin and diffuse correlation spectroscopy (DCS) to measure relative blood flow [23]. The advantage of NIRS is the high optical contrast and relatively high penetration depth (about centimeters into soft tissues). However, the spatial resolution is relatively low due to strong optical scattering, and some compromised tissues such as wounds or heterogeneous regions cannot be imaged due to contact probes and point-by-point measurements [36].

Another imaging technique termed optical-resolution photoacoustic microscopy (OR-PAM) has been newly developed to noninvasively image microvasculature with high spatial resolution (lateral resolution of ~5μm and axial resolution of ~15μm) [24]. Functional parameters, such as oxygen saturation and total concentration of hemoglobin, are estimated by multi-wavelength photoacoustic method, and the blood flow velocity is estimated based on photoacoustic Doppler bandwidth broadening effect [25]. OR-PAM utilizes fine optical focusing to achieve high spatial resolution with the sacrifice of imaging depth less than 1 mm. In addition, the detectable flow velocity is limited (<12mm/s) due to low laser repetition rate [25].

Above all, none of the single modalities can fulfill all of aforementioned requirements for MRO_2 estimation. However, there are some techniques good for either blood flow or oxygen saturation estimation separately. Here we aimed to combine and take advantage of Doppler ultrasound and photoacoustic microscopy for MRO_2 estimation as they share the same ultrasonic detection.

2.2. Doppler Ultrasound

Doppler ultrasound is widely used to detect and quantify blood flow for clinical diagnosis of vascular diseases and tumors [37]. In this section, principles and instrumentations of Doppler ultrasound are reviewed, and signal processing strategies of color Doppler ultrasound, which we selected for flow velocity estimation, are explained in detail.

2.2.1. The Doppler principle

The Doppler equation that characterizes the frequency change produced by a scatterer moving at a constant flow velocity v can be expressed as [38]:

$$f_D = f_R - f_T = -\frac{2|v|}{c_0} f_0 \cos \theta, \tag{2.3}$$

where c_0 is the speed of sound, $|v|$ is the speed of the moving scatterer, f_0 is the transmitted frequency, and θ is referred to as the Doppler angle between the axis of flow direction and the incident ultrasound beam. A simplified sketch is shown in Fig.2.1 when the transmitter and receiver lie on the same location. In Eq.(2.3), the negative sign indicates that the received frequency f_R is less than the transmitted frequency f_T when flow is away from the source.
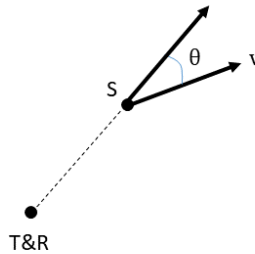
Fig.2.1 Doppler shift produced by a scatterer moving at a constant velocity v

T&R: transmitter and receiver, S: Scatterer, θ: Doppler angle

2.2.2. Characteristics and spectral analysis of the Doppler signal

Spectral analysis of the Doppler signal can provide information concerning the underlying hemodynamics. The blood flow can be modeled as a suspension of scatterers flowing in a cylindrical tube with inner radius R, and the flow velocity profile can be given by [38]:

$$v(r) = v_{max}\left[1 - \left(\frac{r}{R}\right)^n\right], \tag{2.4}$$

where n characterizes the flow velocity profile and v_{max} is the flow velocity at the center. Parabolic flow conditions correspond to $n = 2$, while $n = \infty$ corresponds to a flat profile. Roevros et al. [39] have studied the relation of the flow velocity profile and the Doppler signal spectrum. For parabolic flow ($n = 2$), the spectrum is flat extending up to a frequency determined by the maximum flow velocity. For a flat flow ($n = \infty$), the profile is a δ-function at maximum Doppler frequency. Brody et al. [40] have shown that if the transmit and receive sensitivity is uniform over the isolated volume and the spectral broadening effect is negligible, the mean Doppler angular frequency can be expressed in terms of the complex power density spectrum of the backscattered signal as:

$$\overline{\omega} = \frac{\int_{-\infty}^{\infty} \omega\Phi(\omega)d\omega}{\int_{-\infty}^{\infty} \Phi(\omega)d\omega}, \tag{2.5}$$

where $\Phi(\omega)$ is the power density spectrum of the sampled complex backscattered signal. Therefore, the mean flow velocity $\overline{v}$ can be estimated using Eq.(2.3) and is independent of the velocity profile $v(r)$. For a cylinder with an inner radius of R, the instantaneous volume flow rate is given by:

$$\overline{F} = \pi R \overline{v}^2. \tag{2.6}$$

Moreover, it has been noted that the sampled backscattered signal is a zero-mean Gaussian random process that can be completely specified by its autocorrelation function.

An ideal Doppler velocity measurement system should have a power spectrum with a δ-function response at the Doppler frequency when measuring a single scatterer moving with a constant velocity [41]. Spectral broadening refers to an increase of the spectral bandwidth, and several sources can be identified. The so-called intrinsic sources include transit-time, geometric, and Brownian motion broadening [38]. Since the contribution of Brownian motion to the overall broadening has been shown to be very small [42], the transit-time and geometric effect are the main causes of intrinsic broadening [43]. Extrinsic broadening refers to effects extrinsic to the Doppler system. The main form arises from a spatial or vector distribution of velocities within the sample volume [38].

Transit-time broadening can be understood by considering the Doppler waveform from a single scatterer is gated by the movement into and out of the sample volume, resulting in a spectral spread about the center frequency. Analysis of the transit-time spectral broadening is based on several assumptions [43]. First, the flow turbulence and velocity gradient are negligible. Second, the frequency resolution of the spectral estimator is sufficient such that the spectrum broadening effect can be measured accurately. The third assumption is that the transit time is governed by the ultrasound beam width instead of the range cell length. As illustrated in Fig.2.2, this assumption is valid when the beam width w is considerably smaller than the range cell length l. In other words, the aspect ratio, defined as l/w, must be sufficiently large. The transit time t_{tr} through the ultrasound beam in the focus can be calculated as:

$$t_{tr} = \frac{w}{v \sin \theta},$$ (2.7)

where v is the single valued flow velocity and θ is the Doppler angle. Since the Doppler bandwidth B_w is inversely proportional to the transit time of a scatterer crossing the ultrasound beam in the focus of a transducer [44], we have

$$B_w = k \frac{v \sin \theta}{w},$$ (2.8)

where k is a scaling factor related to the thresholds used to define B_w and w. For a focused transducer with cylindrical symmetry, Censor et al. [45] have shown that the bandwidth can be obtained by:

$$B_w = \frac{2 f_0}{c_0} \frac{D}{F} v \sin \theta,$$ (2.9)

where D is the transducer aperture and F is the focal length. Thus if B_w and Doppler angle θ are known, the flow velocity v can be calculated from Eq.(2.9).
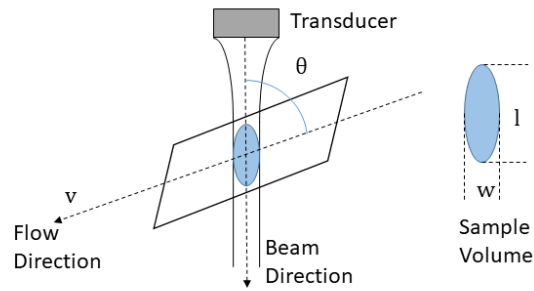
Fig.2.2 Schematic of Doppler angle and sample volume geometry

v: single valued flow velocity, θ: Doppler angle, l: range cell length, w: ultrasound beam width

2.2.3. Doppler ultrasound systems and instrumentations

The simplest form of Doppler ultrasound is the continuous-wave (CW) Doppler ultrasound. In CW systems, the transducer employs two elements: one to transmit continuous ultrasound waves, the other to receive returning echoes with Doppler frequency shift [46]. The sample volume is determined by the transducer geometry and tends to largely envelop the entire cross-section of the blood vessel. With narrow bandwidth and relatively large sample volume, CW systems can achieve a better signal to noise ratio (SNR) than for pulsed-wave systems [38]. Relatively inexpensive and portable, CW systems are used primarily at the bedside for the assessment of superficial structures. Moreover, since there is no upper limit of detectable velocities, CW Doppler ultrasound is also used in adult cardiac scanners to investigate very high velocities in aorta [47].

Although CW Doppler ultrasound can provide better SNR than for pulsed-wave Doppler ultrasound, some limitations should be addressed as well. The use of a long-duration multi-cycle transmitted pulse causes the spatial resolution in the axial direction to be diminished [38]. Unlike pulsed-wave measurements, CW Doppler ultrasound has limited depth discrimination, which means when the sample volume intersects more than one vessel, the Doppler signal can be seriously corrupted [46]. Moreover, CW Doppler ultrasound is not suitable for real-time two-dimensional velocity estimation.

Pulsed-wave (PW) Doppler ultrasound is currently used in most diagnostic applications. In PW systems, the transducer is used for both transmitting and receiving. A sequence of modulated ultrasound pulses is transmitted at a certain pulse-repetition-frequency (PRF) and the backscattered

signals from moving scatterers are detected and demodulated. Although this technique is often described as a Doppler technique, it does not make use of the Doppler shift on each transmitted pulse, but rather generates estimates of velocity from the phase shifts or time delays between echoes from the same sample volume during subsequent pulses [38]. Velocity estimation methods include time-shift cross-correlation and phase-shift auto-correlation techniques [48] [27]. Estimation of the distance traveled by a scatterer in a specified interval of time forms the basis of time-shift cross-correlation method. A significant advantage of this method in comparison to methods based on frequency or phase is the elimination of aliasing. However, if the target is blood, signal de-correlation between successive PRF must be sufficiently small that the time delay can be reliably estimated [48]. Phase-shift auto-correlation method, also referred to as Kasai estimator, is based on estimating the phase shift between successive received signals by using an auto-correlation algorithm [27]. This method has relatively small bias and variances, especially under some poor SNR conditions that are often encountered in practice. So far both methods have been successfully implemented in commercial systems for real-time two-dimensional flow estimation and imaging.

2.2.4. Color Doppler ultrasound imaging

Color Doppler ultrasound is an imaging technique that combines anatomical information derived from standard ultrasound imaging with velocity information derived using pulsed-wave Doppler techniques to generate color-coded maps of flow velocity superimposed on grey-scale B-mode images of tissue anatomy [49]. The velocity of the target can be calculated from phase shifts or time delays using the same equation that is used to interpret the true Doppler shift found in CW ultrasound as Eq.(2.3). In our work, we selected phase-shift auto-correlation estimator (Kasai estimator) for flow estimation.

As discussed in Section 2.2.2, for a distribution of scatterers, the received radio frequency (RF) signal has a mean Doppler angular frequency $\bar{\omega}$ that is related to the spatial mean flow velocity $\bar{v}$:

$$\bar{v} = \frac{c_0 \bar{\omega}}{2\omega_0 \cos\theta},$$
(2.10)

where ω_0 is the transmitted angular frequency. Denoting the standard deviation of the Doppler spectrum with σ, the variance σ^2 can be represented by the following [40]:

$$\sigma^2 = \frac{\int_{-\infty}^{\infty}(\omega-\bar{\omega})^2\Phi(\omega)d\omega}{\int_{-\infty}^{\infty}\Phi(\omega)d\omega}. \tag{2.11}$$

Based on Wiener-Khinchin relation which provides a fundamental link between the time and frequency domain properties of complex processes:

$$R(\tau) = \frac{1}{2\pi}\int_{-\infty}^{\infty}\Phi(\omega)e^{j\omega\tau}d\omega, \tag{2.12}$$

where the auto-correlation function $R(\tau)$ and the power density spectrum $\Phi(\omega)$ is a Fourier transform pair. Since the velocity of the target can be assumed constant during the interval between two pulses T, the phase derivative is approximately given by [50]:

$$\bar{\omega} = \frac{\Phi(T)}{T} = \frac{1}{T}\tan^{-1}\left\{\frac{Im[R(T)]}{Re[R(T)]}\right\}, \tag{2.13}$$

and the variance can be written as：

$$\sigma^2 = \frac{2}{T^2}\left[1 - \frac{|R(T)|}{R(0)}\right]. \tag{2.14}$$

Eq.(2.13) and Eq.(2.14) show that the mean angular frequency and the variance of the Doppler signal can be estimated from the magnitudes and phases of the auto-correlation function at lags of zero and T. The mean flow velocity can be calculated from Eq.(2.10).

A major problem of color Doppler ultrasound is that only the axial flow component can be detected. The projection of the velocity vector onto the transverse direction does not produce a Doppler shift. As discussed in Section 2.2.2, according to Eq.(2.9), the transverse flow velocity component can be found using Doppler spectral broadening. When $\theta = 0°$, the transverse flow velocity can be expressed as:

$$v_{\parallel} = \frac{c_0}{2f_0}\frac{F}{D}B_w. \tag{2.15}$$

Instead of calculating the bandwidth B_w based on the complete Doppler spectrum [51], the variance of the spectrum is used to approximate the square of the Doppler bandwidth [27]. Thus B_w can be calculated from:

$$B_w = \frac{\sqrt{2}}{T}\left[1 - \frac{|R(T)|}{R(0)}\right]^{1/2}. \tag{2.16}$$

2.2.5. Critical velocities

Phase-shift auto-correlation estimator requires that the sampling frequency must exceed the Doppler frequency itself to avoid aliasing but cannot be so high that little phase-change takes place between adjacent samples, in which case the velocity estimate is associated with a large variance. According to these requirements, three critical velocities can be identified [38]. The first relates the velocity at which aliasing first occurs. According to the Nyquist sampling criterion, for the demodulated frequency to be unambiguously determined, two or more samples must be obtained within one period of the transmitted center frequency. This criterion enables the maximum velocity transmitted in the beam direction to be calculated as:

$$v_{max} = \pm \frac{c_0 f_{PRF}}{4 f_0 \cos \theta}. \tag{2.17}$$

The second concerns the minimum velocity that can be successfully distinguished from clutter. Since at least one period of the transmitted waveform must be sampled, the scatterers would have moved a distance of $\Delta z = N v \cos \theta$ over N transmissions (N is referred to the Doppler ensemble size). The minimum velocity is given by:

$$v_{min} = \pm \frac{c_0 f_{PRF}}{2 N f_0 \cos \theta}, \tag{2.18}$$

Moreover, if the transmitted waveform consists of M cycles of the center frequency, and there are N transmissions, the minimum velocity can be expressed as:

$$v_{min} = \pm \frac{c_0 M f_{PRR}}{2 N f_0 \cos \theta}. \tag{2.19}$$

By choosing appropriate PRF and Doppler ensemble size, color Doppler ultrasound is capable of imaging a wide range of flow velocities.

2.2.6. Power Doppler ultrasound imaging

Different from color Doppler, power Doppler ultrasound imaging displays the power level of backscattered signals from moving scatterers instead of flow velocity. The intensity in a power Doppler image is proportional to the number of scatterers moving within a vascular volume, rather than the frequency shifts they generate, which means that it is not prone to aliasing artifacts and insensitive to Doppler angles [52]. The increased sensitivity to blood flow detection and angle

independent feature make power Doppler ultrasound particularly useful for imaging blood volume fractions, especially for small and irregular vessels. High frequency (>20MHz) power Doppler ultrasound has been used to assess micro-vascular density and angiogenesis in preclinical small animal models [53]. In our work, power Doppler images were used to estimate the cross-sectional area of the blood vessel for blood flow rate calculations.

2.2.7. Wall filtering

One of the most challenging aspects of color Doppler imaging is the rejection of echoes from stationary or slowly moving tissues, which can be much stronger than those from the intended moving target. This is particularly so where the target is blood, in which case the unwanted clutter signal from solid tissues can exceed the signal from blood by 40-60dB [54] [55]. Therefore, wall filtering to reject clutter signals is necessary before velocity estimation.

Since the signal scattered by the rapidly moving blood cells has a larger Doppler frequency shift than the signal reflected from stationary or slowly moving tissues, a high-pass filter with a steep transition band can be used. Both step-initialized and exponentially-initialized infinite impulse response (IIR) wall filters effectively suppress any signal components caused by scatterers with velocities below ~0.1mm/s [56]. However, the limitation of such filters is that they do not address the time-varying tissue motion, especially when the Doppler frequencies generated by the tissue motion exceed the cut-off frequencies. To deal with such time-varying signals, eigen-filters have been proposed to base the wall filter on the statistics of the clutter signal so that the response can be adapted to the tissue motion [57]. The received RF signal can be modeled as a sum of three independent zero-mean complex Gaussian processes: a clutter component, a blood component, and additive white noise. Being Gaussian, the signal is completely characterized by its correlation matrix, given by:

$$R_x = R_c + R_b + \sigma_n^2 I, \tag{2.20}$$

where R_c is the clutter correlation matrix, R_b is the blood correlation matrix, σ_n^2 is the noise variance, and I is the identity matrix. To ensure that the properties of the signal correlation are constant over depth, the correlation matrix R_x is limited to a small acquisition window with N pulses and L samples in depth. To separate the clutter and noise into their respective subspaces, the m-th sub-matrix $R^{(m)}$ is analyzed using the discrete Karhunen-Loeve transform (DKLT) [58].

DKLT can be used for non-stationary processes, unlike discrete Fourier transform (DFT), which is a special case of the DKLT. $R^{(m)}$ is eigen-decomposed as:

$$R^{(m)} = E\Lambda E^H, \tag{2.21}$$

where $E = [e_1, e_2 \dots e_L]$ is the $N \times N$ unitary matrix of eigenvectors, and $\Lambda = \text{diag}(\lambda_1, \lambda_1 \dots \lambda_N)$ is the $N \times N$ diagonal matrix of eigenvalues which are sorted in decreasing amplitude ($\lambda_1 \geq \lambda_1 \dots \geq \lambda_N$). The eigenvalue spectrum is a generalization of the Fourier power spectrum, which represents the power distribution of the frequency components. The power of blood echoes is small compared with the clutter so that the blood component subspace is contained within the noise subspace. Since the power of clutter signals arising from tissues are much higher than other components, we can partition the clutter subspace and blood subspace by choosing the appropriate filter order:

$$\Lambda = \begin{bmatrix} \Lambda_r & 0 \\ 0 & \Lambda_{N-r} \end{bmatrix}, \tag{2.22}$$

where r is the filter order. The corresponding clutter filter can be designed to eliminate the clutter signal. In our work, we used eigen-filter as the wall filter to reject clutter signals before Kasai velocity estimator and power calculations. Appropriate filter order is determined experimentally to give the best trade-off between clutter rejection and preservation of flow.

2.3. Photoacoustic Imaging

2.3.1. Photoacoustic wave generation

Photoacoustic effect is the physical basis for photoacoustic imaging. It refers to the generation of acoustic waves by the absorption of electromagnetic energy [59]. Non-ionizing waves, such as short laser pulses are often used to excite megahertz ultrasound waves in biological tissues. When the tissue is irradiated by a short-pulsed laser beam, locally absorbed pulse energy is converted into heat, which is further converted to a pressure rise via thermoelastic expansion [60]. The initial pressure rise, determined by the local optical energy deposition and other thermal and mechanical properties, propagates as an ultrasonic wave, which is also referred to as a photoacoustic wave. Then the photoacoustic wave is detected by an ultrasound transducer to determine the optical properties of the target.

To generate photoacoustic signals efficiently, the laser pulse duration t_L should be less than the acoustic confinement time τ_s, which is less than the thermal confinement time τ_{th}. The acoustic confinement time τ_s characterizes the pressure propagation in the heated area and can be expressed as $\frac{d_c}{c_0}$, where d_c is the characteristic dimension of the optically absorbing target of interest, and c_0 is the speed of sound. The thermal confinement time τ_s characterizes the thermal diffusion of the absorbed optical energy and can be expressed as $\frac{d_c^2}{4\alpha_{th}}$, where α_{th} is the thermal diffusivity about $0.1 mm^2/s$ for tissue. Thus, the thermal and stress confinements can be shown as [60]:

$$t_L < \frac{d_c}{c_0} < \frac{d_c^2}{4\alpha_{th}}. \tag{2.23}$$

If Eq.(2.23) is satisfied, a pressure rise p_0 immediately after the laser excitation can be expressed as [61]:

$$p_0 = \left(\beta c_0^2 / C_p\right)\mu_a\Phi = \Gamma\mu_a\Phi, \tag{2.24}$$

where β is the isobaric volume expansion coefficient in K-1, C_p is the specific heat in J/ (K kg), μ_a is the absorption coefficient in cm-1, λ is the transmitted optical wavelength, and Φ is the local light fluence in J/cm2. $\Gamma = \beta c^2 / C_p$, is defined as the Gruneisen coefficient. Since the speed of sound and thermal coefficient of volume expansion are both temperature dependent, the Gruneisen parameter is temperature dependent. An empirical formula can be used to estimate Gruneisen parameter for water and aqueous solution as [62]:

$$\Gamma_w(T) = 0.0043 + 0.0053T, \tag{2.25}$$

where T is the temperature in degree Celsius. Thus, the strength of photoacoustic signals is proportional to optical absorption coefficient, local optical fluence, Gruneisen parameter, and is related to temperature.

2.3.2. Photoacoustic imaging

Photoacoustic imaging refers to imaging that is based on the photoacoustic effect. The motivation for photoacoustic imaging is to combine optical contrast with ultrasonic spatial resolution for deep imaging (> 1mm) in biological tissues. Due to strong optical scattering in soft tissues, the spatial resolution of pure optical imaging degrades significantly with depth greater than 1mm [62]. Since

ultrasound scattering is two to three orders of magnitude weaker than optical scattering, photoacoustic imaging can image deeper tissues (>1mm) where diffusion photons are absorbed and provide better spatial resolution than optical imaging. Moreover, since the absorption spectrum changes with the molecule decomposition, photoacoustic imaging can be used to image certain physiological parameters, such as the oxygen saturation of hemoglobin and concentration of the hemoglobin to provide functional information [63].

Currently two major implementations of photoacoustic imaging have been actively studied: photoacoustic microscopy (PAM) and photoacoustic tomography (PAT) [59]. Typical PAT uses an unfocused ultrasound detector/array and inverse algorithms to reconstruct volumetric images of biological samples [64]. Technically, each temporal photoacoustic signal measured at various detection positions provides 1D radial information, and 2D surface scans offer other 2D lateral information about the photoacoustic source. Combining the temporal and spatial measurements is sufficient for a complete 3D reconstruction. PAT provides more flexibility in dealing with measured photoacoustic signals than the image forming methods with focused transducers or focused lenses that have fixed imaging regions. However, the spatial resolution is usually limited to several hundreds of micrometers due to the low ultrasound frequency [65]. Since PAM works in a reflection mode, higher ultrasonic frequencies can be used to achieve better spatial resolution than PAT.

Different from reconstruction-based computed PAT, PAM employs raster-scanning of optical and acoustic foci and forms images directly from acquired depth-resolved signals without inverse reconstruction algorithms [60]. Each detected signal upon a laser pulse excitation can be converted into a 1D image (A-scan) along the acoustic axis of the transducer. Combining multiple A-scans acquired sequentially on the same plane forms cross-sectional B-scan images, and 2D raster scanning generates 3D photoacoustic images (C-scan). PAM maximizes its detection sensitivity by confocally aligning its optical illumination and acoustic detection [66]. While the axial resolution of PAM is primarily determined by the imaging depth and the frequency response of the ultrasonic transducer, its lateral resolution is determined by the combined point spread function of the dual foci. Based on whether the optical or ultrasonic focus is finer, PAM is further divided into optical-resolution PAM (OR-PAM) [67] and acoustic-resolution PAM (AR-PAM) [68]. Within the optical diffusion limit (<1mm), OR-PAM has a great advantage over AR-PAM in

spatial resolution because the optical beam can be easily focused to a much finer spot than acoustic detection. The lateral resolution of OR-PAM is determined by the size of the optical focus and has been reported to achieve 5μm for *in vivo* imaging of microvasculature and single capillaries in mice [67]. Moreover, OR-PAM can also be used to image functional parameters in microcirculation [69]. Beyond the optical diffusion limit (>1mm), however, AR-PAM can achieve a better focusing by taking advantage of the weaker acoustic scattering. AR-PAM is typically implemented in a dark-field reflection mode [68]. The excitation laser beam has a donut-shaped cross-section, and the photoacoustic signal from the tissue surface in the field of view is minimized. The lateral resolution of AR-PAM is determined by the focal diameter of the ultrasonic transducer at the center frequency. Maslov et al. have demonstrated a dark-filed AR-PAM system with a 50MHz focused ultrasonic transducer to achieve 45μm lateral resolution [68]. For axial resolution, OR-PAM and AR-PAM share the same formula and is inversely related to the bandwidth of the ultrasonic transducer.

In our work, AR-PAM has shown the following capabilities. First, it breaks through the current fundamental depth limitation (~1mm) of OR-PAM, as well as pure optical imaging modalities such as confocal microscopy and optical coherence tomography (OCT). Second, it overcomes the poor spatial resolution of diffuse optical tomography (DOT) at the depth beyond limitation (>1mm). Third, it is well suited to image vascular structures and capable of functional imaging based on physiologically specific endogenous optical absorption contrasts.

2.3.3. Functional photoacoustic microscopy

Optical absorption in tissues is a function of molecular composition. For example, the absorption spectrum of hemoglobin changes when binding occurs [62]. Based on endogenous optical contrast, photoacoustic signals can be used to derive a number of physical, chemical and functional parameters of absorbers. Since oxy-hemoglobin (HbO_2) and deoxy-hemoglobin (Hb) are two of the major absorbers in blood, PAM is well suited for functional imaging of oxygen saturation of hemoglobin (sO_2) and total concentration of hemoglobin (C_{THb}), two important parameters for tissue MRO_2 estimation.

PAM estimates sO$_2$ in the same way NIRS does, where HbO$_2$ and Hb are treated as the dominant absorbers at each wavelength (λ_i). The blood absorption coefficient $\mu_a(\lambda_i)$ (cm-1) at wavelength λ_i can be expressed as:

$$\mu_a(\lambda_i) = \varepsilon_{Hb}(\lambda_i)C_{Hb} + \varepsilon_{HbO_2}(\lambda_i)C_{HbO_2}, \qquad (2.26)$$

where $\varepsilon_{Hb}(\lambda_i)$ and $\varepsilon_{HbO_2}(\lambda_i)$ are the known molar extinction coefficients (cm-1M-1) of Hb and HbO2 at wavelength λ_i, respectively. C_{Hb} and C_{HbO_2} are the concentrations of these two forms of hemoglobin. The photoacoustic signal amplitude emitted from a subsurface location x is proportional to the local optical absorption coefficient $\mu_a(x, \lambda_i)$, local optical fluence $\Phi(x, \lambda_i)$, and the Gruneisen parameter $\Gamma(x)$:

$$p(x, \lambda_i) = \Gamma(x)\Phi(x, \lambda_i)\mu_a(x, \lambda_i). \qquad (2.27)$$

Often the Gruneisen parameter is assumed to be a constant Γ. By interrogating the tissue with at least two optical wavelengths, we solve the following matrix equation to obtain $C_{Hb}(x)$ and $C_{HbO_2}(x)$:

$$\begin{bmatrix} p(x,\lambda_1) \\ p(x,\lambda_2) \\ \vdots \\ p(x,\lambda_n) \end{bmatrix} = \Gamma \begin{bmatrix} \Phi(x,\lambda_1)\varepsilon_{Hb}(\lambda_1) & \Phi(x,\lambda_1)\varepsilon_{HbO_2}(\lambda_1) \\ \Phi(x,\lambda_2)\varepsilon_{Hb}(\lambda_2) & \Phi(x,\lambda_2)\varepsilon_{HbO_2}(\lambda_2) \\ \vdots & \vdots \\ \Phi(x,\lambda_n)\varepsilon_{Hb}(\lambda_n) & \Phi(x,\lambda_n)\varepsilon_{HbO_2}(\lambda_n) \end{bmatrix} \begin{bmatrix} C_{Hb}(x) \\ C_{HbO_2}(x) \end{bmatrix} \qquad (2.28)$$

Often the local optical fluence is unknown to us. Two approaches are taken to solve this equation. The first approach involves assuming that the fluence is a wavelength-independent constant. The second approach uses a separate photoacoustic experiment and some highly absorbing black dye to estimate a factor proportional to the sub-surface wavelength-independent fluence. In either case, a least-squares approach using the Moore-Penrose pseudo-inverse can be used to solve for $\hat{C}_{Hb}(x)$ and $\hat{C}_{HbO_2}(x)$. The oxygen saturation is then calculated as:

$$sO_2(x) = \frac{\hat{C}_{HbO_2}(x)}{\hat{C}_{HbR}(x)+\hat{C}_{HbO_2}(x)} \times 100\%. \qquad (2.29)$$

As discussed, this method suffers from unknown wavelength-dependent fluence $\Phi(x, \lambda_i)$ which is often assumed a constant or requires wavelength-dependent calibration. Recently another method has been proposed to use multi-wavelength photoacoustic measurements at different sO2 levels

and solve a system of equations to estimate the different sO$_2$ levels [70]. Briefly, the absorption coefficients given two sO$_2$ levels can be written as:

$$\mu_{a1}(x, \lambda_1) = \left(\varepsilon_{Hb}(\lambda_1)\left(1 - sO_2^{(1)}(x)\right) + \varepsilon_{HbO_2}(\lambda_1)sO_2^{(1)}(x)\right)C_{THb}(x) \tag{2.30}$$

$$\mu_{a2}(x, \lambda_2) = \left(\varepsilon_{Hb}(\lambda_2)\left(1 - sO_2^{(2)}(x)\right) + \varepsilon_{HbO_2}(\lambda_2)sO_2^{(2)}(x)\right)C_{THb}(x) \tag{2.31}$$

Here $C_{THb}(x)$ is the total concentration of hemoglobin. Thus, sO$_2$ at the respective time points can be estimated from photoacoustic measurements as

$$sO_2^{(1)} = \frac{bp_2(\lambda_1) - ap_2(\lambda_2)}{p_1(\lambda_2)p_2(\lambda_1) - p_1(\lambda_1)p_2(\lambda_2)} \tag{2.32}$$

$$sO_2^{(2)} = \frac{bp_1(\lambda_2) - ap_1(\lambda_1)}{p_1(\lambda_2)p_2(\lambda_1) - p_1(\lambda_1)p_2(\lambda_2)} \tag{2.33}$$

with

$$a = \frac{(p_1(\lambda_1) - p_2(\lambda_1))\varepsilon_{Hb}(\lambda_1)}{\varepsilon_{HbO_2}(\lambda_1) - \varepsilon_{Hb}(\lambda_1)} \tag{2.34}$$

$$b = \frac{(p_1(\lambda_2) - p_2(\lambda_2))\varepsilon_{Hb}(\lambda_2)}{\varepsilon_{HbO_2}(\lambda_2) - \varepsilon_{Hb}(\lambda_2)}. \tag{2.35}$$

This method requires no wavelength-dependent fluence calibration factor but assumes that the optical properties of tissue between the vessels of investigation and the tissue surface do not change their optical properties.

Total concentration of hemoglobin (C_{THb}) can be estimated at the isosbestic wavelengths of hemoglobin, for example at 568nm or 794nm. The photoacoustic signal amplitude reflects the C_{THb} distribution in relative values regardless of the oxygen level of hemoglobin. However, since the photoacoustic signal is also related to local laser fluence, a phantom calibration or additional correction is needed to obtain the absolute C_{THb}.

Implementations of functional PAM have been demonstrated by many groups. Fig.(2.3) shows a representative system developed by Zhang et al. [1]. This system consists of three major subsystems: a tunable pulsed laser system, an imaging head mounted on mechanical scanner and a data acquisition system. The laser system uses a tunable dye laser that is pumped by a Q-switched Nd:YAG laser as the irradiation source, which has a pulse duration of 6.5ns and a pulse repetition

rate of 10Hz. The imaging head consists of four major components: a multi-axis fiber positioner with a focusing lens, a conical lens, an optical condenser and a focused 50MHz ultrasonic transducer. The laser beam from the fiber passes through a conical lens to provide a ring-shaped area of illumination. It is then weakly focused into the tissue with the focal region coaxially overlapping the ultrasonic focus inside the tissue. In an optically clear medium, the optical focus is 2mm in diameter, which is much wider than the ultrasonic focus. The optical illumination on the tissue surface is donut shaped with a dark center, referred to as dark field illumination, so that no strong photoacoustic signals are produced there within the ultrasonic field of view. The photoacoustic wave is recorded at each location of the ultrasonic transducer and subsequently converted into a 1D depth-resolved image (A-scan) based on the sound velocity in soft tissue. Then, raster scanning of the dual optical-ultrasonic foci in a horizontal (x-y) plane with a step size of 50μm produces a 3D image.
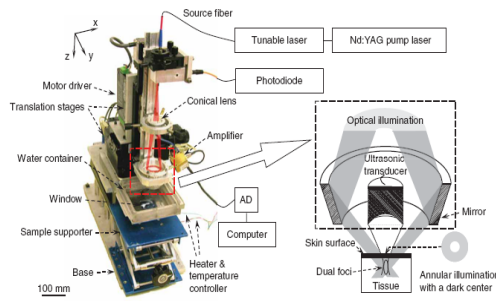
Fig.2.3 Functional photoacoustic microscopy system [1]

2.4. Proposed Data Processing Workflow

As shown in Fig.2.4, the proposed data processing workflow to estimate MRO_2 include the Doppler velocity estimation and blood oxygen saturation estimation using multi-wavelength photoacoustic method. Detailed will be explained in Chapter3, 4, and 5.
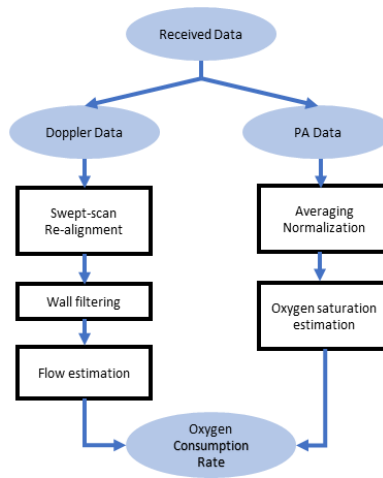
Fig.2.4 Proposed data processing workflow

3. Photoacoustic and High-Frequency Power Doppler Ultrasound Biomicroscopy: A Comparative Study

3.1. Introduction

Photoacoustic microscopy (PAM) is a hybrid imaging technique which combines high optical contrast and high ultrasonic spatial resolution at imaging depths much greater than optical microscopy methods [59]. When nanosecond-duration laser pulses are transmitted into biological tissues, wideband ultrasonic waves are emitted as a result of optically induced thermoelastic expansion. The magnitude of the received photoacoustic (PA) signal is proportional to optical absorption, the time of flight of the signal is proportional to depth of the absorbing structures, and the resolution is determined by ultrasonic detection considerations. Visualization of microvasculature is important to diagnose many diseases. Since blood is more absorbing than surrounding tissues at certain wavelengths, there is significant endogenous contrast available for PA imaging of microvascular structures. Maslov *et al.* [68] and Zhang *et al.* [1] have demonstrated a dark-field confocal PAM system for subcutaneous microvasculature visualization. With known absorption spectra of oxy- and deoxy-hemoglobin, PAM can be used to image blood oxygen saturation (sO_2) as well as relative concentration of total hemoglobin (C_{THb}). This has been demonstrated by Zhang *et al.* among others [1] [63].

Power Doppler ultrasound imaging is a technique which displays the backscatter strength of moving blood to identify regions of blood flow. This is in contrast to color Doppler ultrasound, a method to estimate and image blood flow speed and direction. The intensity of power Doppler images is proportional to the number of scatterers moving within a vascular volume, rather than the frequency shifts they generate [52], which means that power Doppler is irrespective of Doppler angles between ultrasound beam and direction of flow. This feature improves the ability of imaging tortuous and irregular blood vessels. While clinical ultrasound systems operate in the 1-15MHz range [71], higher frequencies (20-100MHz) have been aimed to provide finer spatial resolution. High frequency (>20MHz) power Doppler ultrasound has been used to assess microvascular density and angiogenesis in preclinical small animal models [53]. However, several limitations should be addressed when using this technique. Firstly, tissues surrounding blood vessels often generate scattered signals much stronger than reflected signals from moving blood, so clutter

filtering is necessary before Doppler power calculations. The performance of power Doppler imaging is dependent on subjective, rather than objective wall filter parameters, and display threshold levels. Secondly, in practice, tissues are not always stationary, and the movement of soft tissues causes signals of high intensity and low frequency. Since detection of small blood vessels with slow flow velocities requires a low wall filter cut-off velocity, these clutter signals can survive wall-filtering and create color pixel artifacts in power Doppler images. The blood volume fraction is hard to interpret in the presence of color pixel artifacts. On the other hand, while wall filters can reject clutter signals, some blood flow signals, especially from the slow velocity flows, can also be rejected. This may decrease the sensitivity of blood flow detection.

We have developed a hybrid PA and high-frequency power Doppler ultrasound imaging system to provide co-registered PA and power Doppler images. Using this system to image flow phantoms, we develop a quantitative and objective methodology to compare the relative performance of power Doppler ultrasound and photoacoustic imaging. While various groups have performed PA and power Doppler imaging separately [1] [72], to our knowledge, no one has combined them and compared them in such a study. The combined system aims take advantage of both modalities to improve image quality of both macro-vasculature (about hundreds of microns in diameter) and micro-vasculature and improve estimation of microvascular density. In this paper, the development of our combined system, as well as signal processing strategies are described. Co-registered PA and power Doppler images acquired from flow phantoms with different combinations of vessel size and mean flow velocity are presented. Blood detection performance of each technique is evaluated by receiver operating characteristic analysis.

3.2. Methods

3.2.1. Experimental system

A block diagram of system instrumentation is shown in Fig.3.1. The entire system can be controlled via a single computer. A combined light delivery and ultrasound probe is mounted on a voice coil positioning stage (VCS-10-023-BS-01, 1.0" travel, 2.3lbs continuous force, 6.9lbs peak force, purchased from H2W technologies, Inc., Valencia, CA). This stage is driven by a programmed motor controller (Elmo Harmonica HAR 5/60, Elmo Motion Control Inc., Nashua, NH, USA) to oscillate at fixed scanning speed. A digital output bit from the motor controller is set

to high for a short duration at the end of each scan trajectory and sent to a digital input-output (DIO) card (NI PCI-6542, National Instruments Inc). This end-of-scan (EOS) trigger is used to mark the beginning of an image frame and trigger the DIO card to generate a pulse-sequence which is sent to the ultrasound pulser/receiver (5073PR, Panametrics, Waltham, MA, USA) and/or laser. The ultrasound pulser/receiver is capable of a repetition rate up to 10kHz and can provide energy up to 16μJ with amplifier gain up to 39dB.
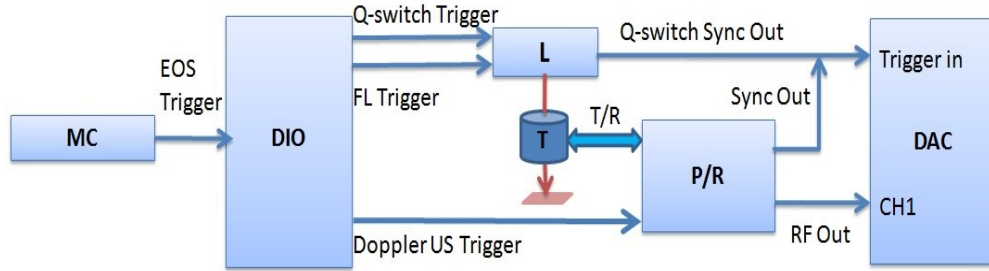
Fig.3.1 Block diagram of the combined PA and Doppler ultrasound system.

MC: Motor Controller; DIO: Digital Input-Output Card; L: Laser; T: Ultrasound Transducer;

P/R: Ultrasound Pulser/Receiver; DAC: Digital Acquisition Card; EOS: End-of-Scan.

Presently, our system can provide several imaging modes, such as ultrasound B-mode, PA mode and Doppler ultrasound mode. In PA mode, the DIO card is triggered by EOS output and then generates a pulse sequence to trigger the laser flash-lamp and Q-switch. It was found that Q-switch triggering in addition to flashlamp triggering was important to reduce laser pulse timing jitter. A Q-switched Nd:YAG laser (Ultra UL 421111, Big Sky Technologies, Bozeman, MT, USA) with a maximum pulse repetition rate of 20Hz was used to obtain 10ns pulse of wavelength 532nm. To provide longer wavelength, a tunable laser system was also used in this study. A tunable optical parametric oscillator (Surelite OPO Plus, Continuum, Santa Clara, CA, USA) was pumped by a Q-switched Nd:YAG laser (Surelite III, Continuum, Santa Clara, CA, USA) with repetition rate of 10Hz. The tuning range is from 410nm to 710nm. PA and Doppler ultrasound modes are combined by using the DIO card to interleave laser and ultrasound triggers so that images can be co-registered.

RF data received by the ultrasound pulser/receiver is digitized by an 8-chanel PCI data acquisition card (CS22G8, Gage Cobra, Gage Applied Systems, Inc.) with 12-bit dynamic range and sampling

rates as high as 125MSamples/s. Acquisition triggers are provided by the sync out signals from the laser Q-switch and ultrasound pulser/receiver.

The aforementioned light delivery probe is based on a confocal dark-field laser illumination approach, with some similarities to the dark-field PAM system first described by Maslov *et al.* [68]. As shown in Fig.3.2, an incident laser beam is reflected by a right-angle prism which is mounted on an acrylic tube with refractive index of 1.46. The downward light is diverted by a polished reflective cone to a 45° polished surface of the tube. Then the reflected light travels downward along the tube and reaches another polished surface which is machined at a certain angle to deflect the light confocally around the transducer focal axis. A 25MHz single element ultrasound transducer (V324-SM, 12.7mm focal length, Panametrics, Waltham, MA, USA) is positioned inside the tube and can be adjusted vertically to match its focus point with the laser focus. In this design, light is focused at ~10.5mm below the bottom of the probe.
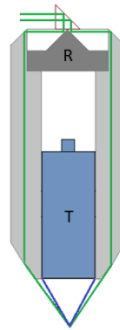
Fig.3.2 Scheme of light delivery probe.
R: Reflective Cone; T: Ultrasound Transducer.

3.2.2. Flow phantom

Experiments were performed on flow phantoms consisting of transparent vessels of 0.2mm and 0.86mm inner diameters (I.D.) embedded in a tissue-mimicking background. Polymer tubing (Paradigm Optics, Vancouver, WA, USA), composed of polyethylene terephthalate glycol (PETG) was used in construction of blood vessels. The inner diameters are representative of small arterioles and small veins [72]. The tissue-mimicking base was mixed with 10% cornstarch and 10% gelatin by weight, which offered an optical reduced scattering coefficient $\mu_s' = 9.2 \text{cm}^{-1}$, similar to human

tissues. The ultrasonic and mechanical properties are also within the range of typical biological tissues referred to previous work [73].

Blood-mimicking fluid was pumped at mean flow velocities of 1mm/s and 5mm/s using a calibrated syringe pump (NE-300 Syringe Pump, New Era Pump Systems Inc., Eantagh, NY, USA). 1mm/s is thought of as typical flow speed in small vessels in the microcirculation. This is also a speed which begins to challenge our Doppler micro-ultrasound system. 5mm/s is simply chosen as a speed significantly above 1mm/s and could be representative of flow in venules or arterioles [72]. The blood-mimicking fluid was composed of 5% by mass cornstarch dissolved in water, which ensures the blood to tissue signal power is consistent with *in vivo* signal levels. To increase the buoyancy of the particles, the mixture was first heated to $100^{o}C$ for several minutes and then cooled to room temperature before using. This fluid was also optically dyed by crystal violet to provide two optical absorption coefficients. One is $250cm^{-1}$ at 532nm, the other is $3.3cm^{-1}$ at 630nm, both of which are similar to human blood. The distance between the vessel and surface of the tissue phantom is 2mm.

3.2.3. Signal processing strategies

PA and power Doppler ultrasound images are co-registered and superimposed on B-mode structural ultrasound images. To generate power Doppler images, steps in the signal processing chain involve signal alignment within and between lines-of-sight, wall filtering, Doppler power calculation and thresholding.

In contrast to systems in which an ultrasonic pulse is repeatedly directed to a discrete line-of-sight, a swept-scan mode is used in our system to continuously scan over the flow phantom. The transducer is positioned over the region of interest, transmits one pulse and is laterally translated by one step within the pulse repetition period. This method can shorten the data acquisition time but may cause signal decorrelations within each line-of-sight due to motion of the transducer. Three correlation-based alignment algorithms have been proposed for compensation purpose: single reference line, incremental, and averaging [74]. The first strategy selects a single pulse within a line-of-sight as reference and aligns other pulses by the relative shifts. The second calculates the relative shifts of consecutive pulses and aligns each pulse with previous one. The third involves averaging the correlation over a set of reference lines. The nature of swept-scan

mode yields itself suitable for incremental method. Within one line-of-sight, the relative shift of consecutive pulses is determined by finding the maximum of the cross-correlation estimate. In our case, interlaced PA signals may aggravate the discontinuities between lines-of-sight, thus we extend this incremental alignment method to better visualize blood vessel continuity. To perform alignment between lines-of-sight, the relative shift between the last pulse of one line-of-sight and the first pulse of the subsequent line-of-sight is first determined. Then the entire block of pulses within the subsequent line-of-sight is shifted by this determined amount.

Wall filters are necessary to reject strong clutter signals from surrounding tissues before Doppler power calculation. Typically, an infinite impulse response (IIR) high pass filter is used to remove slowly changing signals corresponding to tissue echoes. The limitation of such filters is that they have poor performance when Doppler frequencies generated by tissue motion exceed the cut-off frequencies. Thus, eigen filters have been proposed to base the clutter filter on the statistics of the clutter signal so that the response can be adapted to the tissue movement. To address the fact that the clutter signal is a non-stationary random process, the Discrete Karhunen-Loeve Transform (DKLT) is used to characterize clutter signals [57]. It decomposes the autocorrelation matrix of received RF data into eigenvectors and eigenvalues, and then eigenvalues are sorted in decreasing amplitude. The eigenvalue spectrum is a generalization of the Fourier power spectrum, which represents energy of signal components. Thus, we can partition clutter signals, blood flow signals, and white noise by their eigenvectors according to this energy spectrum and eliminate the clutter noise by choosing appropriate filter order. Details refer to Section 2.2.7.

After wall filtering, the intensity of signals from moving blood is accumulated within each Doppler ensemble to generate power Doppler image. By Doppler ensemble, we mean a sequence of N pulses, the echoes from which are processed to form one power Doppler A-scan line.

3.2.4. Receiver operating characteristic analysis

Receiver operating characteristic (ROC) analysis can be used as a means of quantifying the performance of both power Doppler and PA imaging modes for the task of detecting blood (in our case blood-mimicking fluid). For each pixel in our images we decide as to whether "blood" is present or absent. One way of making such a decision is to threshold the power Doppler or PA image. In practice, values above the threshold are color-coded (and thus classified as "blood-

present") and the color-coded image is overlaid on a gray-scale ultrasound B-scan for structural context. By setting the threshold very low, a large number of color pixels may appear throughout the power Doppler (or PA) image due to noise, clutter, or other artifacts. Thus, a low-threshold will yield a large fraction of true positives, but also a large number of false positives. A high threshold value may decrease the number of false positives, but at the expense of true positives. The trade-off between sensitivity and specificity can be graphically represented by a ROC curve which plots the true-positive fraction (TPF) vs. the false-positive fraction (FPF) as the threshold-level is varied from minimum to maximum. While we are interested ultimately in the estimation task of quantifying fractional blood volume in a region (which estimate can be thought of as the sum of the true positives and false positives), we note that thresholding can greatly impact this estimate. Moreover, to compare the performance of power Doppler and PA imaging modes, different threshold levels could be used for each mode. By comparing ROC curves for each mode (for different vessel sizes and flow conditions), we are able to objectively compare respective detection performances for the entire spectrum of possible threshold values. The area under the ROC curves (AROC) is used as a summary figure of merit to evaluate the detection performance of the two imaging modes.

3.3. Results

3.3.1. Flow phantom experiments

To demonstrate the performance of our combined system, flow phantoms with different vessel sizes were imaged by cross-sectional scans. Acoustic coupling was achieved by immersing flow phantoms in a water bath. The transducer was positioned so that the focus was 2mm below the surface of the flow phantoms. The following acquisition settings were used in all experiments: 4 cycle pulse length, 39dB receiver gain, and 16μJ transmit energy. The motion controller was programmed to drive the voice coil scanning at a speed of 0.5mm/s, which provides a distance of 25μm between each line-of-sight. System specifications and experiment conditions are listed in Table.3.1. Scan speed and Doppler ensemble size are inversely related because the transducer is swept continuously during acquisition. The pulse repetition frequency (PRF) was set to 200Hz when the laser was triggered at 20Hz (the PRF was set to 100Hz when the laser was triggered at 10Hz), yielding a Doppler ensemble size of 10. When acquiring interleaved PA and Doppler signals, the trigger delay of the data acquisition card was set to 6μs and the length of acquisition

window was set to 20µs, which allows a capture of 8.5mm axial depth in both PA and power Doppler modes. The lateral distance of one scan trajectory was 10mm. Interlaced data were separated to form individual PA, B-mode and power Doppler ultrasound images. Then PA and power Doppler images were co-registered and superimposed on the B-mode ultrasound images with structural contents.

Table.3.1 System Specifications and Experiment Conditions

Parameter	Value
Transducer Center frequency	25MHz
Sampling frequency	100MHz
Optical wavelength	532nm, 630nm
Laser pulse repetition rate	20Hz, 10Hz
Doppler pulse repetition rate	200Hz, 100Hz
Ensemble size	10
Dynamic range	12bits
Scan speed	0.5mm/s
Inner diameters (I.D.) of vessels	0.86mm, 0.2mm
Flow velocities	5mm/s, 1mm/s
Eigen order	1-4

Table.3.1 System specifications and experiment conditions

Co-registered power Doppler and PA images acquired from the flow phantom with 0.86mm vessel diameter are shown in Fig.3.3 and Fig.3.4. Appropriate regions of interest (ROI) are selected so that the blood volume fractions can be displayed in the center of ROI. The dimensions of ROI include a depth of 2.5mm from top to bottom, and a total lateral distance of 2.5mm.

Fig.3.3 shows power Doppler images acquired at mean flow velocities of 5mm/s (Fig.3.3(a)) and 1mm/s (Fig.3.3(b)), and co-registered PA images acquired at 532nm (Fig.3.3(c)). In power Doppler mode, the cross section of blood vessel is well imaged at high flow velocity (5mm/s, Fig.3.3(a)), but hard to interpret at 1mm/s due to color pixel artifacts (Fig.3.3(b)). In PA mode, only the top surface can be well visualized because of the minimal light penetration depth in the vessel (Fig.3.3(c)).
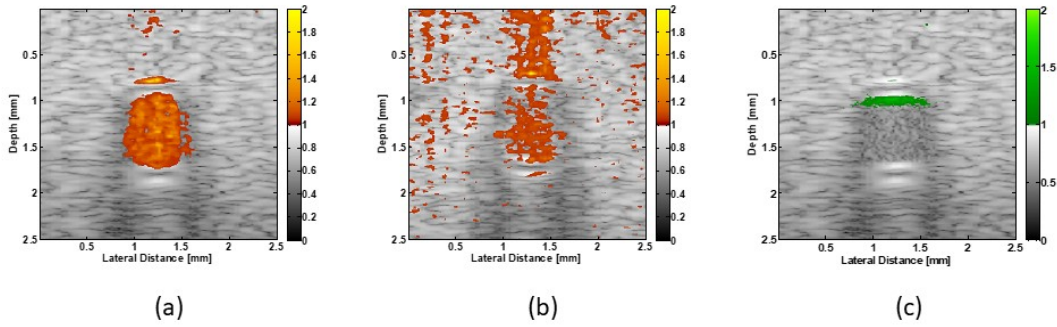
Fig.3.3 Co-registered power Doppler and PA images of the flow phantom with 0.86mm vessel size.

(a) Power Doppler image at 5mm/s (b) Power Doppler image at 1mm/s (c) PA image at 532nm

To show longer penetration depth in PA image, we repeated our experiment on 0.86mm flow phantom using 630nm wavelength. Fig.3.4 shows the PA image acquired at 630nm (Fig.3.4(c)), and co-registered power Doppler images (Fig.3.4(a) and Fig.3.4(b)). In comparison to Fig.3.3(c), Fig.3.4(c) shows that a deeper penetration has been achieved, but the entire cross section of the vessel is still hard to see.
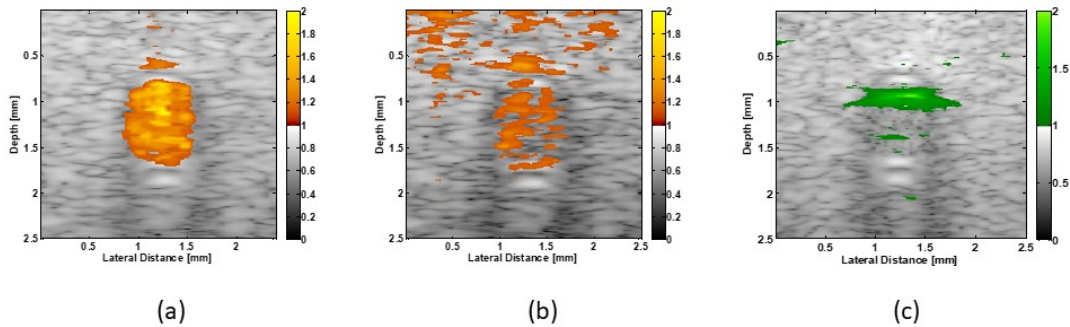
Fig.3.4 Co-registered power Doppler and PA images of the flow phantom with 0.86mm vessel size.

(a) Power Doppler image at 5mm/s (b) Power Doppler image at 1mm/s (c) PA image at 630nm

Fig.3.5 shows the co-registered power Doppler and PA images acquired from the flow phantom with 0.2mm vessel diameter. The ROI is 1.2mm by 1.0mm. The mean flow velocity is 5mm/s (Fig.3.5(a)) and 1mm/s (Fig.3.5(b)). The optical wavelength is 532nm. As shown in Fig.3.5(a) and Fig.3.5(b), power Doppler imaging has a good detection performance at small vessel size (0.2mm)

and high flow velocity, but poor performance at slow flow velocity (1mm/s). However, this small vessel can be easily detected in the PA image (Fig.3.5(c)).

(a)

(b)

(c)
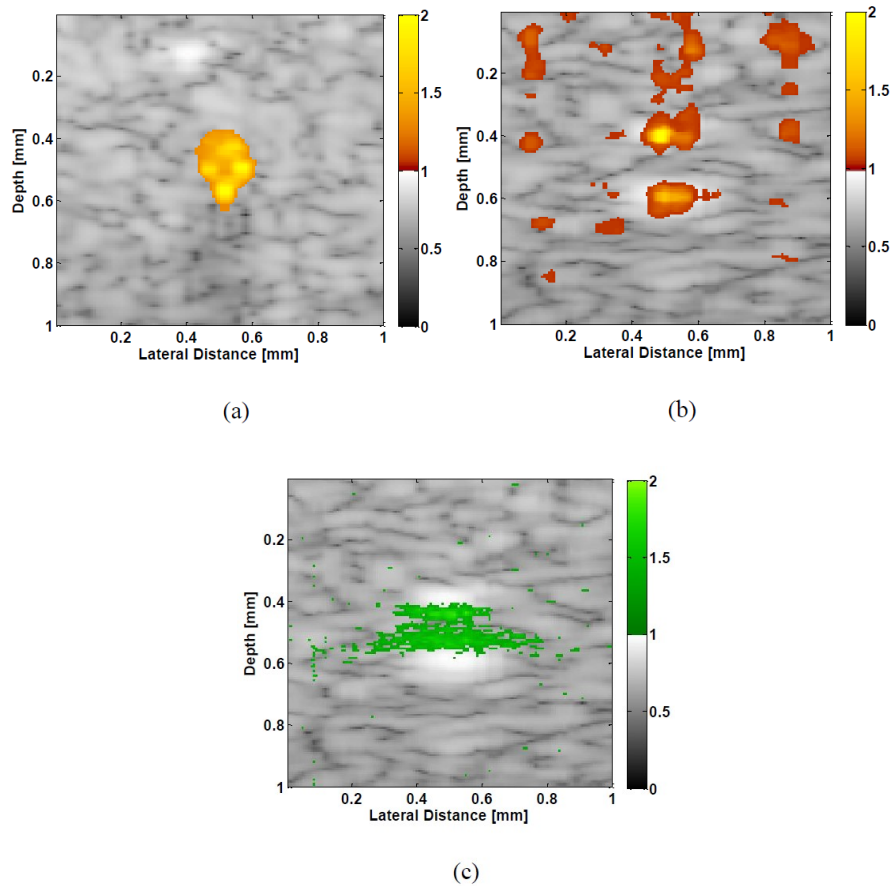
Fig.3.5 Co-registered power Doppler and PA images of the flow phantom with 0.2mm vessel size.

(a) Power Doppler image at 5mm/s (b) Power Doppler image at 1mm/s (c) PA image at 532nm

3.3.2. Image analysis

ROC curves generated from both power Doppler and PA images at different vessel sizes, mean flow velocities and optical wavelengths are shown in Fig.3.6. Inspection of these individual ROC curves provides objective evaluation of blood flow detection performance of our combined system. Fig.3.6(a) shows the ROC analysis of power Doppler and PA images acquired at 0.86mm I.D. and 532nm. The color thresholds are varied through the range of values which ensure that the full ROC curve is populated. As shown in Fig.3.6(a), the power Doppler image acquired at 5mm/s produces

an ROC curve which is consistently higher than the PA-ROC curve, indicating that power Doppler can provide a better estimation of blood volume fraction at 5mm/s compared to the PA mode. The ROC curve generated from 1mm/s power Doppler image moves close to 45-degree diagonal line, which means that the detection accuracy and sensitivity decreases at low flow velocity. Fig.3.6(b) shows the ROC analysis of power Doppler and PA images acquired at 0.86mm I.D. and 630nm. The PA-ROC curve generated from 630nm is higher than the one from 532nm, which is due to the longer penetration depth. Fig.3.6(c) shows the ROC analysis when the vessel diameter is 0.2mm. While the ROC curve generated from 1mm/s power Doppler image lies almost along the diagonal line, the PA-ROC curve traverses through more of the upper left-hand quadrant of the ROC space. This is consistent with what we observe from the images, i.e. that PA imaging provides a better blood volume detection performance compared to power Doppler at small vessel size and slow flow velocity.
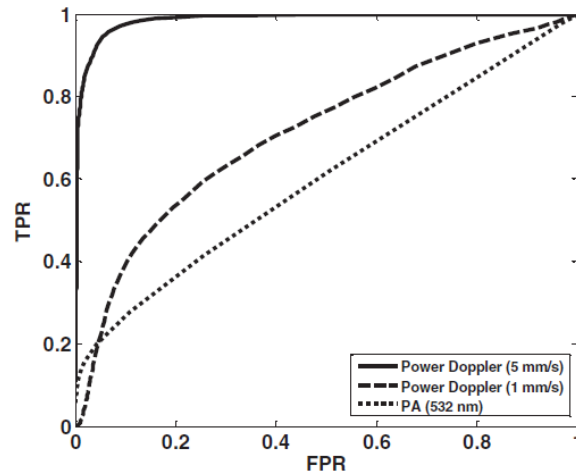
(a)
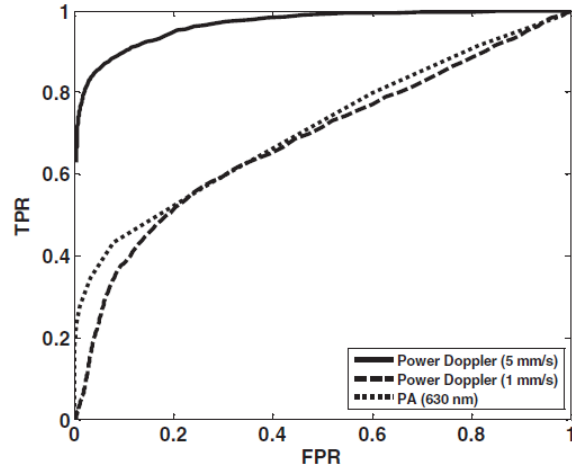
(b)
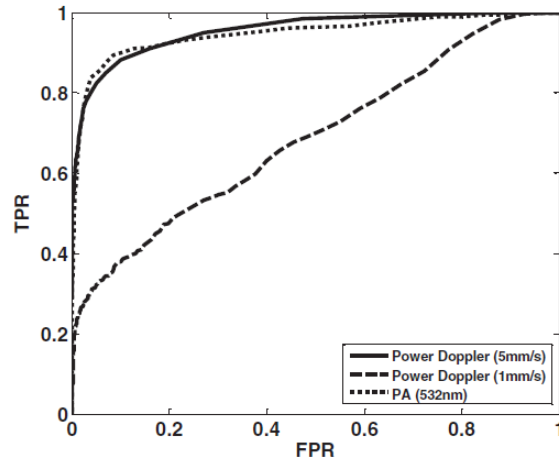
(c)

Fig.3.6 ROC curves generated from PA and power Doppler images acquired at different vessel sizes and optical wavelengths.

(a) 0.86mm, 532nm (b) 0.86mm, 630nm (c) 0.2mm, 532nm.

TPR: True Positive Rate, FPR: False Positive Rate.

The AROC values at different conditions are calculated using trapezoidal rule and shown in Table.3.2. When the vessel diameter is 0.86mm, the AROCs demonstrate that good estimation of blood volume fraction, defined by AROC > 0.90, can be achieved by power Doppler image at high

flow velocity (5mm/s). For small vessel size of 0.2mm and slow flow velocity of 1mm/s, PA image has an AROC of 0.95, indicating a good performance of blood volume detection.

Table.3.2 AROC for PA and power Doppler images

Vessel Diameter	0.86 mm	0.86 mm	0.2 mm
Mean flow velocity	5 mm/s	1 mm/s	1 mm/s
PA	0.63	0.64	0.95
Power Doppler	0.97	0.75	0.65

3.4. Discussion

To generate ROC curves, a circular region is fit so that the edges of the circle correspond to the maximum intensity points of the tubing inner-wall in ultrasound B-mode image. *In vivo*, there may not be such obvious wall signals, however, it provides us with a gold-standard for a phantom study.

The ROC analysis demonstrates that power Doppler imaging has good detection performance for large blood vessel (0.86mm) and high flow velocity (5mm/s). However, the penetration depth of PA imaging may be limited at shorter wavelength (532nm) so that it may not reveal the cross section of large blood vessel. Thus, a longer wavelength (630nm) was used in this study (Fig.3.4(c)). The optical penetration depth is estimated as ~3mm, which is much longer than the size of the vessel. However, even in this case, the entire cross-section of the vessel cannot be well visualized in PA image. There might be two key points to explain this: (1) light intensity will still decay appreciably in the vessel (the light intensity decay is estimated as ~25% by Beer's law), (2) PA signals are band-pass filtered by the electro-mechanical response of the transducer. As such, absorption edges are seen better than slowly-varying regions (which have low frequency components). To explain this better, note that the PA image could be modeled as:

$$p(x) = psf(x) * (\Gamma(x)\Phi(x)\mu_a(x)), \tag{3.1}$$

where $psf(x)psf$ is the point-spread function, $\Gamma(x)$ is the Gruneisen parameter, $\mu_a(x)$ is the optical absorption coefficient, and $\Phi(x)$ is the local fluence. If the vessel is uniformly illuminated, $\Phi(x)$ can be viewed as a constant. The $psf(x)$, however, will have a band-pass response in the depth-

direction due to the electro-mechanical response of the transducer. Low spatial frequencies present in large absorbing structures may not survive band-pass filtering. Thus, obtaining good B-mode PA images of large vessels may be difficult due to the reasons discussed above (i.e. light penetration and band-pass filtering response of the transducer). As shown in Fig.3.4, even at 630nm, power Doppler does outperform PA for large vessel size (0.86mm) and high flow speed (5mm/s). For large vessel size (0.86mm) but low flow velocity (1mm/s), probably longer-wavelength PA would be advantageous. A broadband transducer which has a wide frequency response can be used to compensate for the loss of lower acoustic frequencies due to band-pass filtering. Also, other Doppler methods such as inter-frame clutter-filtering could be advantageous at the expense of power Doppler false-positives associated with tissue motion artifacts [75].

The ROC analysis also demonstrates that, for small blood vessel (0.2mm), power Doppler imaging has good detection performance for high flow velocity (5mm/s), but poor performance for slow flow velocity (1mm/s). PA imaging has a good detection performance (Fig.3.5(c)) for small vessel, however, the lateral resolution and side-lobe levels of PA imaging may provide an undesirable false-positive rate.

Combination of these two modalities offers advantages over either technique used alone. As no one set of power Doppler or PA parameters (pulse-repetition rates, optical wavelengths, thresholds, etc.) will be successful at estimating fractional blood volume accurately for all vessels (large and small, high and low flow velocities), by understanding the relative merits of both techniques, it may be possible to improve our ability to estimate fractional blood volume by careful selection of PA or power Doppler parameters. This combined PA and Doppler ultrasound system is also capable of color Doppler imaging and sO_2 estimation. One long term goal of our research is to use this system for noninvasive visualization of the metabolic rate of oxygen consumption (MRO_2) *in vivo*. MRO_2 is an important indicator of metabolic activities to diagnose cancer and diabetes. It is defined as the amount of oxygen consumed in a given tissue region per unit time per 100g of tissue or of the organ of interest and may be estimated in terms of the mean flow rate of vessels (mean flow velocity times vessel cross-sectional area), total concentration of hemoglobin C_{HB}, and the difference between the sO_2 of blood flowing into and out of a bounded tissue region [17]. Since mean flow velocity can be measured by color Doppler ultrasound, vessel cross-sectional area can be measured by power Doppler imaging or structural PA imaging, and functional PAM can be

used to estimate sO_2 and C_{THb}, all of these parameters necessary for MRO_2 estimation can be provided by our combined system.

3.5. Conclusion

We have developed a combined photoacoustic and high-frequency power Doppler ultrasound system which allows co-registered photoacoustic and power Doppler images. Experiments have been performed on flow phantoms with various combinations of vessel size, mean flow velocities and optical wavelengths. ROC analysis is used to compare detection performance of the PA and power Doppler imaging modes. Images with accompanying ROC analysis have been presented. Work in progress involves color flow mapping and *in vivo* performance based on our combined system. Future work will develop multi-wavelength PA micro-vessel imaging. With the ability to estimate blood flow velocity and oxygen saturation, we will devise estimators for computing metabolic rate of oxygen consumption.

4. Blood Oxygen Flux Estimation with a Combined Photoacoustic and High-Frequency Ultrasound Microscopy System: A Phantom Study

4.1. Introduction

The rate of oxygen consumption (MRO_2) is an important indicator of tissue metabolic activity. The ability to accurately image MRO_2 non-invasively will impact research and clinical practice relating to cancer [2], diabetes [76], congestive heart failure [16] and many other diseases relating to oxygen metabolism. MRO_2 is defined as the amount of oxygen consumed in a given tissue region per unit time per 100g of tissue or the organ of interest [17]. It can be estimated by quantifying the net oxygen flux of the blood vessels entering or exiting a defined tissue region. Blood oxygen saturation (sO_2), mean flow speed and cross-sectional area of the blood vessel are the key parameters to estimate the local oxygen flux of a single vessel. Presently, techniques to obtain MRO_2 are limited. Near-infrared optical methods have been developed to measure MRO_2 with the blood flow information provided by the diffuse correlation spectroscopy (DCS) and blood oxygenation information provided by diffuse reflectance spectroscopy (DRS) [22]. However, the spatial resolution is poor due to optical scattering. Positron Emission Tomography (PET) with ^{15}O-oxygen has been used to measure oxygen consumption [20], but typical spatial resolution is ~1cm for clinical systems, and ~1mm for small animal systems. Magnetic resonance imaging (MRI) plays an important role in noninvasive measurement of MRO_2 by utilizing the Blood Oxygenation-Level Dependent (BOLD) effect [21]. BOLD MRI can provide high spatial resolution, but it is only sensitive to deoxy-hemoglobin and has trouble distinguishing between changes in sO_2 and blood flow. Moreover, PET and MRI are not well suited for many bedside clinical applications and can be cost-prohibitive.

Photoacoustic microscopy (PAM) is a novel technique which may provide a new way to image MRO_2. Photoacoustic imaging involves transmitting short laser pulses into biological tissues producing rapid heating in optically-absorbing structures, and detecting ultrasonic waves induced by thermo-elastic expansions. The strength of received PA signals is proportional to optical absorption, and the spatial resolution depends on ultrasonic detection. Maslov *et al.* [68] developed the first dark-field confocal PAM system with a 50MHz transducer, demonstrating a lateral

resolution of 45μm. Recently, an alternative technique termed optical-resolution PAM (OR-PAM) utilizes the fine optical focusing to achieve high lateral resolution (~5μm) with sacrifice of the imaging depth (<~1mm) [67]. The lateral resolution is determined by the size of a raster-scanned optical focal spot, and the axial resolution is still derived from time-resolved ultrasonic detection. Since oxy-hemoglobin (HbO_2) and deoxy-hemoglobin (Hb) are two of the major absorbing chromophores in human blood, and the optical absorption of blood is dependent on its oxygenation status, PAM is well suited to the imaging of vascular structures from macro vessels all the way down to individual capillaries [17] [67], and capable of functional imaging of sO_2 by multi-wavelength measurements. Zhang *et al.* [63] have demonstrated *in vivo* imaging of microvasculature with high spatial resolution and sO_2 of single vessels in animals and total concentration of hemoglobin (C_{THb}) in humans. Combined PAM and optical coherence tomography (OCT) method has been proposed to estimate MRO_2 *in vivo*, with sO_2 measured by OR-PAM and blood flow speed measured by spectral-domain OCT [77].

There are many potential methods to estimate the flow velocity and blood volume fraction. Recently, photoacoustic Doppler flowmetry has been proposed to measure transverse flow velocity based on Doppler bandwidth broadening, and the structural information of the flow can be provided as well [25]. Yao *et al.* have developed metabolic photoacoustic microscopy system for simultaneously imaging sO_2 and blood flow speed to quantify MRO_2 *in vivo* [24]. However, the detectable flow speeds (<12mm/s) are limited by the low laser pulse repetition rate, and the imaging depth is shallow (<~1mm). In our work, we propose to implement high-frequency Doppler ultrasound for flow estimation. High frequency ultrasound is considered to include frequencies above ~20MHz. The small beam size and large bandwidth provide high spatial resolution, which is important for imaging small animal models in preclinical research [52]. Pulsed color Doppler ultrasound transmits ensembles of ultrasound pulses and estimates flow velocities from detected phase shifts in received echoes. By choosing appropriate pulse-repetition frequency (PRF) and Doppler ensemble length, color Doppler ultrasound is capable of imaging a wide range of flow velocities. However, like other flowmetries based on the Doppler frequency shifts, the blood flow is hard to identify when the Doppler angle approaches 90°. Moreover, the noise signal with a low power but wide frequency spread can be displayed in color Doppler images as random velocities in random directions, which may appear as a mosaic of colors masking real vascular signals. In contrast to color Doppler, the technique of power Doppler ultrasound displays the

backscatter strength of moving blood instead of flow velocities and directions. The intensity of power Doppler images is proportional to the number of scatterers moving within a vascular volume, rather than the frequency shifts they generate [52]. The increased sensitivity to blood flow detection and angle independent feature of power Doppler ultrasound make it particularly useful for imaging blood volume fractions even for tortuous vessels. For small vessels with low flow speeds which are hard to detect by Doppler ultrasound, our previous work shows that photoacoustic imaging is more effective than power Doppler for the detection of blood [78].

The long-term goal of our research is to develop photoacoustic and ultrasonic imaging methods for non-invasive estimation of MRO_2 *in vivo*. We recently developed a combined photoacoustic and high-frequency ultrasound microscopy system with a swept-scan 25MHz transducer and confocal dark-field laser illumination optics [78] [79]. Previously we demonstrated the use of this system for interlaced photoacoustic and power Doppler imaging modes. In this article, along with our recent conference publication [80], we add color Doppler flow imaging to our system's capabilities. Since the mean flow speed can be estimated using color Doppler ultrasound, vessel cross-sectional area can be quantified from power Doppler or photoacoustic images, sO_2 and C_{THb} can be estimated using multi-wavelength photoacoustic methods, our combined system is able to provide all of the parameters necessary for blood oxygen flux estimation. The accuracy of the flow velocity and sO_2 estimation has been investigated. *In vitro* sheep blood phantom experiments have been performed at different sO_2 levels and mean flow speeds. We also experimentally demonstrate for the first time the feasibility of imaging local blood oxygen flux of a single vessel by combining photoacoustic oximetry and color Doppler ultrasound.

4.2. Methods

4.2.1. Experimental system

Our customized imaging system incorporates a computer-controlled scanning, triggering and data acquisition system, and a combined light delivery and ultrasound probe based on confocal dark-field laser illumination optics. Readers are referred to our previous work [78] [79] for specific details about the instrumentations, explanations on light delivery probe and imaging procedures. In brief, a digital-input-output (DIO) card (NI PCI-6542, National Instruments, Inc., USA) is used to generate a pulse sequence that is sent to the ultrasound pulser/receiver (5073PR, Panametrics,

Waltham, Massachusetts) and/or laser to enable different imaging modes. Currently our system can provide ultrasound (US) B-mode, photoacoustic (PA) mode, and Doppler US mode. In PA mode, a tunable optical parametric oscillator (Surelite OPO Plus, Continuum, Santa Clara, California) is pumped by a Q-switch Nd:YAG laser (Surelite III, Continuum, Santa Clara, California) with a repetition rate of 10Hz. The tuning range is from 410nm to 710nm. PA and Doppler US modes are combined by using the DIO card to interleave laser and US triggers so that images can be co-registered. A 25MHz single element transducer (V324-SM, 12.7mm focal length, Panametrics, Waltham, Massachusetts) is positioned inside the light delivery probe and can be adjusted vertically to match its focus point with the laser focus. Radio frequency (RF) data received by the US pulser/receiver is digitized by an eight channel PCI data acquisition card (CS8289, Gage Cobra, Gage Applied Systems, Inc., USA) with 12-bit dynamic range and sampling rates as high as 125MSamples/s.

4.2.2. Principles of multi-wavelength PAM for oxygen saturation estimation

As illustrated in Section 2.3.3, by interrogating the tissue with at least two optical wavelengths, we solve the following matrix equation to obtain $C_{Hb}(x)$ and $C_{HbO_2}(x)$, concentrations of two forms of hemoglobin:

$$\begin{bmatrix} p(x, \lambda_1) \\ p(x, \lambda_2) \\ \vdots \\ p(x, \lambda_n) \end{bmatrix} = \Gamma \begin{bmatrix} \Phi(x, \lambda_1)\varepsilon_{Hb}(\lambda_1) & \Phi(x, \lambda_1)\varepsilon_{HbO_2}(\lambda_1) \\ \Phi(x, \lambda_2)\varepsilon_{Hb}(\lambda_2) & \Phi(x, \lambda_2)\varepsilon_{HbO_2}(\lambda_2) \\ \vdots & \vdots \\ \Phi(x, \lambda_n)\varepsilon_{Hb}(\lambda_n) & \Phi(x, \lambda_n)\varepsilon_{HbO_2}(\lambda_n) \end{bmatrix} \begin{bmatrix} C_{Hb}(x) \\ C_{HbO_2}(x) \end{bmatrix} \tag{4.1}$$

Often the local optical fluence is unknown to us. In this paper we take two approaches to solve this equation. The first approach involves assuming that the fluence is a wavelength-independent constant. The second approach uses a separate PA experiment and some highly absorbing black dye to estimate a factor proportional to the sub-surface wavelength-independent fluence. In either case, a least-squares approach using the Moore-Penrose pseudo-inverse can be used to solve for $\hat{C}_{Hb}(\mathbf{x})$ and $\hat{C}_{HbO_2}(\mathbf{x})$. The oxygen saturation is then calculated as:

$$sO_2(\mathbf{x}) = \frac{\hat{C}_{HbO_2}(\mathbf{x})}{\hat{C}_{Hb}(\mathbf{x}) + \hat{C}_{HbO_2}(\mathbf{x})} \times 100\%. \tag{4.2}$$

4.2.3. Signal processing strategies of Doppler ultrasound

Since tissues surrounding blood vessels often generate scattered signals much stronger than reflected signals from moving blood, clutter filtering is necessary before velocity estimation and power calculations. We use an eigen-filter which is designed based on the statistics of the clutter so that the response can be adapted to the tissue movement. The correlation matrix of the received RF data is decomposed into eigenvectors and eigenvalues by the discrete Karhunen-Loeve transform (DKLT), and then eigenvalues are sorted in decreasing amplitude. The eigenvalue spectrum is a generalization of the Fourier power spectrum, which represents the power distribution of the frequency components [57]. Since the power of clutter signals arising from stationary tissue is much higher than other components, we can partition the clutter subspace and eliminate clutter signals by choosing appropriate filter order. Appropriate filter order is determined experimentally by picking the filter order (typically 2-3) which gives the best trade-off between clutter rejection and preservation of flow. Details refer to Section 2.2.7.

The combined system uses a swept-scan mode to continuously scan over the imaging target. This method can shorten the data acquisition time, but the mechanical scan may cause changes of the amplitude and phase of the received signals, producing a gradual de-correlation. In this case, some clutter signals may pass through the filter and the velocity estimator may interpret them as blood flow. Hence signal alignment is important before wall filtering. Within one line-of-sight, the peak magnitude of the cross-correlation between each adjacent pulse pair is found, and the alignment can be achieved by shifting each of the pulses by the determined amount [74].

The technique for velocity estimation is the auto-correlation technique introduced by Kasai *et al.* [27]. A sequence of A-mode RF signals is obtained from transmissions in the same beam direction, and the flow velocity is calculated using the phase shift information. The Doppler ensemble length is determined by the scan speed and ultrasound PRF. The maximum and minimum detectable velocities are related to PRF and Doppler ensemble length. After signal alignment and wall filtering, the intensity of the signals from moving blood is accumulated within each Doppler ensemble to generate power Doppler images.

4.2.4. Oxygen flux and MRO_2 estimation

The oxygen content in blood is the summed contribution of oxygen that is dissolved in plasma and chemically bound to hemoglobin in red blood cells. The amount of oxygen carried in each form depends on the partial pressure of oxygen (pO_2) to which each medium is exposed to. Since the solubility of oxygen is limited in plasma, the specialized oxygen-binding mechanism of hemoglobin is the major means of transporting oxygen in blood. As shown in Eq.(4.3), the gas-phase equivalent volume (in ml) of oxygen carried by hemoglobin per ml of blood can be quantified as [30]:

$$\rho_{O_2,Hb} = \zeta \times C_{THb} \times sO_2, \tag{4.3}$$

here ζ is the oxygen-binding capacity of hemoglobin. From previous study [30], when hemoglobin is completely saturated with oxygen, ζ is 1.34ml/g hemoglobin which means that each gram of hemoglobin will bind with 1.34ml oxygen. The unit of C_{THb} is g/ml. Oxygen dissolved in plasma, despite its lower transport capacity, plays an important role for cells. In small capillaries, oxygen in plasma can diffuse through capillary walls and into cells for aerobic metabolism. According to Henry's law, the gas-phase equivalent volume (in ml) of dissolved oxygen per 100ml of blood can be quantified by the equation [30]:

$$\rho_{O_2,plasma} = \alpha_{O_2}(T) \times pO_2, \tag{4.4}$$

where α_{O_2} with a unit of ml(oxygen)/100ml(blood)/mmHg is the solubility coefficient of the oxygen in plasma dependent on temperature (T), and the unit of pO_2 is mmHg.

The blood oxygen flux is defined as the volume of oxygen content transported per unit time. According to Eq.(4.3) and Eq.(4.4), for a single vessel model, the oxygen flux can be expressed as:

$$\Phi_{O_2} = A \times \bar{v} \times (\zeta \times C_{THb} \times sO_2 + \alpha_{O_2}(T) \times pO_2/100), \tag{4.5}$$

where Φ_{O_2} is the oxygen flux (ml/min), A is the cross-sectional area of the blood vessel, and $\bar{v}$ is the mean flow speed. If a region of interest is well defined, for N feeding vessels and M draining vessels, MRO_2 can be expressed as:

$$MRO_2 = [\sum_i^N \Phi_{O_2}{}^{in}(i) - \sum_j^M \Phi_{O_2}{}^{out}(j)]/w, \tag{4.6}$$

where w is the weight of the region of interest (in gram). The relative uncertainty of blood oxygen flux estimation can be determined by the relative uncertainties of sO_2, C_{THb}, $\bar{v}$ and A. Simply, based on the assumption of error independence, for a single vessel model (N=1):

$$\frac{\delta\Phi_{O_2}}{\Phi_{O_2}} = \sqrt{\left(\frac{\delta sO_2}{sO_2}\right)^2 + \left(\frac{\delta C_{THb}}{C_{THb}}\right)^2 + \left(\frac{\delta A}{A}\right)^2 + \left(\frac{\delta\bar{v}}{\bar{v}}\right)^2}, \tag{4.7}$$

Where δ denotes an error quantity. Uncertainty due to measurement variability can be quantified by measuring sO_2, C_{THb}, $\bar{v}$ and A repeatedly and estimating standard deviations.

4.2.5. Phantom study

Experiments were performed on flow phantoms with the objective to show the feasibility of imaging blood oxygen flux using our combined PA and high-frequency US microscopy system. Transparent polymer tubing (Paradigm Optics, Vancouver, Washington) with inner diameter (I.D.) of 0.86mm was used in construction of blood vessels. This inner diameter is representative of small arteries and small veins [72]. Six vessels were evenly positioned on an acrylic holder and embedded ~2mm deep in a tissue-mimicking base. The tissue-mimicking base was composed of 10% cornstarch and 10% gelatin by mass, which provided an optical reduced scattering coefficient $\mu_s' = 9.2cm^{-1}$ at 532nm, similar to human tissues. The ultrasonic and mechanical properties are also within the range of typical biological tissues [73].
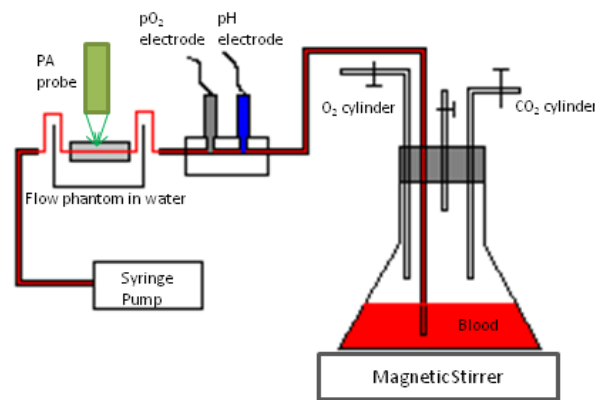

Fig.4.1 Experimental setup of the *in vitro* phantom experiment using sheep blood

4.2.6. Double-Ink studies

To determine the accuracy of flow velocity and sO_2 estimation, phantom studies were conducted using double-ink blood-mimicking fluid with both ultrasonic scattering and optical absorption. The double-ink experiments provide a good first step towards oxygen flux estimation because all parameters regarding flow and mock-sO_2 can be easily controlled. The blood-mimicking fluid was prepared by dissolving 5% (by weight) cornstarch in water, which ensures the blood to tissue signal power consistent with *in vivo* signal levels. Red and blue ink samples (fiesta red and lake placid blue, Private Reserve Ink, IN) were diluted by the blood-mimicking fluid and mixed in various volumetric ratios to mimic different levels of sO_2. The fraction of the red ink concentration in the total ink concentration is termed mock-sO_2. Independent measurements of the optical absorption spectra of the ink samples were performed using a spectrometer (USB4000 Miniature Fiber Optic Spectrometer, Ocean Optics Inc., USA). The double-ink blood-mimicking fluid was pumped through corresponding vessels at different flow rates using a calibrated syringe pump (NE-300 Syringe Pump, New Era Pump System Inc., USA), and imaged by our combined system.

4.2.7. Sheep blood studies

To demonstrate the capability of imaging blood oxygen flux, *in vitro* phantom experiments were performed using freshly collected arterial sheep blood with anti-coagulant CPDA-1 (Citrate Phosphate Dextrose Adenine) solution. Fig.4.1 shows the experimental setup. The blood was loaded into a flask with a four-hole stopper. Pure oxygen and pure carbon dioxide flowed into the flask at different ratios of flow rates to obtain various sO_2 levels. The blood of certain sO_2 was withdrawn from one hole to a corresponding vessel of the flow phantom at different flow rates. Since the actual sO_2 is unknown, to validate sO_2 estimation, pO_2 was measured simultaneously when the blood flow was imaged by the combined system. An airtight acrylic mold was designed to hold the pO_2 electrode (DO_166MT-1 Micro Dissolved Oxygen Electrode, Lazar Research Laboratories, Inc., USA) as well as the temperature compensated pH electrode (HI9126 pH/ORP meter, Hanna Instruments, USA) securely with the electrode tip completely immersed in blood.

The relationship between sO_2 and pO_2 is determined by the oxy-hemoglobin dissociation curve (OHDC), which demonstrates the nonlinear tendency for oxygen to bind to hemoglobin. Eq. (4.8) is the classic OHDC equation developed by Kelman [81]:

$$sO_2 = \frac{a_1 x + a_2 x^2 + a_3 x^3 + x^4}{a_4 + a_5 x + a_6 x^2 + a_7 x^3 + x^4},$$ (4.8)

where x is pO_2 (mmHg) in standard condition (temperature $T = 37°C$, pH = 7.4, and carbon dioxide partial pressure $pCO_2 = 40$mmHg). Measurements conducted in other temperature or pH can be converted to standard condition by Eq. (4.9) and Eq. (4.10):

$$x = f(T, pH, pCO_2) \times pO_2,$$ (4.9)

$$f = 10^{[-0.024(T-37)+0.40(pH-7.4)-0.06(\log_{10} pCO_2 - \log_{10} 40)]}.$$ (4.10)

Coefficients a1 to a7 in Eq. (4.8) are determined by fitting the equation in the least-squares sense to paired values of sO_2 and pO_2.

4.3. Results

4.3.1. Co-registered images acquired from double-ink flow phantom

The flow phantom was immersed in water and imaged by cross-sectional scans at a speed of 0.5mm/s, which provides 50μm between each line-of-sight. The Doppler angle was 75°. Double-ink blood-mimicking fluid with 4 different mock-sO_2 levels (20%, 40%, 60%, and 80%) was pumped through corresponding vessels at different flow rates. The mean flow speed is calculated from the volumetric flow rate divided by the cross-sectional area of the vessel. The mean flow speeds above 20mm/s represent the blood flow in small arteries, and the speed range below 10mm/s represents the flow in small veins down to large capillaries. Considering the slow scan speed, the Doppler ensemble length was chosen to be 10. Appropriate PRFs were set to ensure that the flow speed was within the detectable range. Optical wavelengths of 560-600 nm in steps of 10nm were employed for sO_2 estimation. A photodiode (DET36A/M, Thorlabs, USA) was used for laser pulse-energy normalization. Interlaced data were separated to form individual PA, B-mode and Doppler US images. Then PA and Doppler images were co-registered and superimposed on the B-mode images with structural context. To better estimate the mock-sO_2, M-mode measurements were repeated 100 times at the location with peak PA signal and the averaged amplitude of PA signals was used in Eq. (4.1).The mean flow speed and cross-sectional area of the vessel were estimated from ultrasound Doppler images.

Fig.4.2 shows representative co-registered power Doppler (Fig.4.2(a)), color Doppler (Fig.4.2(b)), PA (Fig.4.2(c)) and mock-sO$_2$ (Fig.4.2(d)) images. The mock-sO$_2$ image (Fig.4.2(d)) was obtained by assigning the estimated sO$_2$ value to a region obtained by thresholding the color Doppler image (Fig.4.2(b)). Appropriate regions of interest are selected so that the cross-sectional area of the vessel can be displayed in the center. The PA image (Fig.4.2(c)) was acquired at 560nm and shows that only the top surface can be well visualized because of the minimal light penetration depth in the vessel. The power Doppler (Fig.4.2(a)) and color Doppler (Fig.4.2(b)) images both show good detection of the blood volume fraction. In practice, Doppler threshold levels will be important to accurately estimate the vessel area.
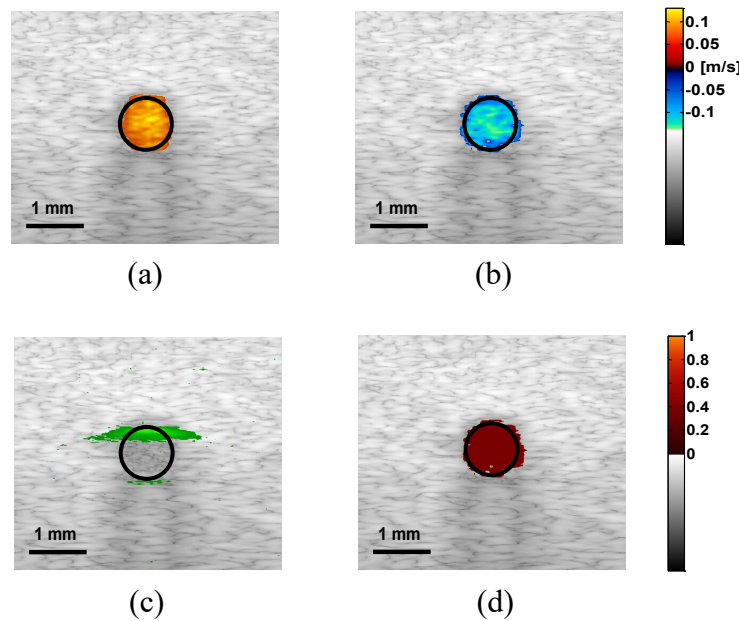
Fig.4.2 Representative co-registered power Doppler, color Doppler, PA and mock-sO$_2$ images of double-ink flow phantom: (a) power Doppler image (b) color Doppler image (c) PA image (d) mock-sO$_2$ image

To demonstrate the performance of color flow estimation, different mean flow speeds were imaged while the mock-sO$_2$ stayed invariant at 40%. Co-registered color Doppler and mock-sO$_2$ images at different mean flow speeds are shown in Fig.4.3.
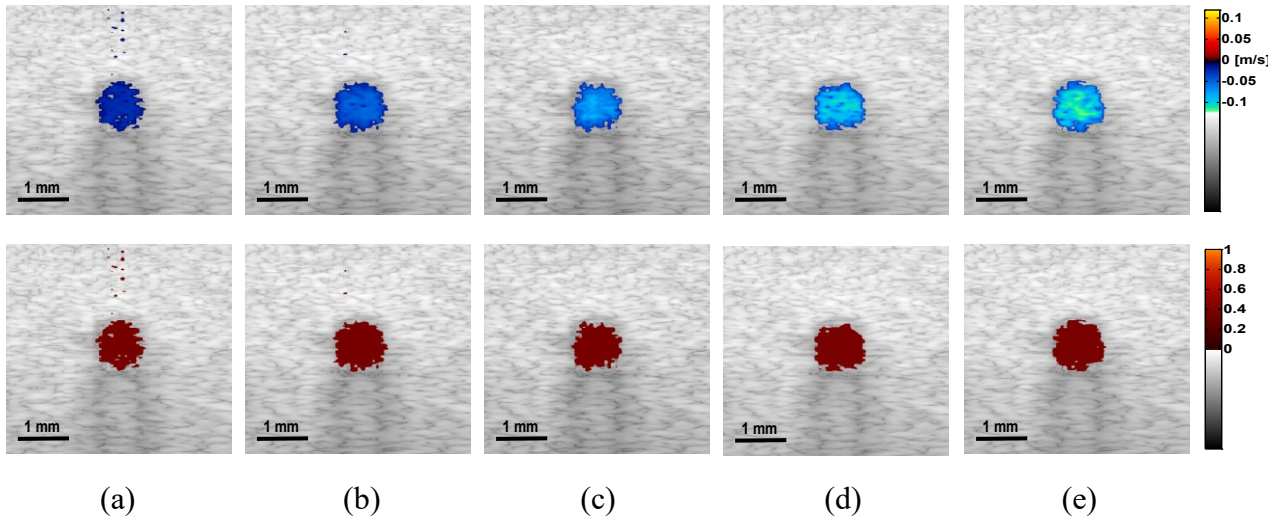
Fig.4.3 Co-registered color Doppler and mock-sO$_2$ images of double-ink flow phantom: (a) 20mm/s, 40% (b) 40mm/s, 40% (c) 60mm/s, 40% (d) 80mm/s, 40% (e) 100mm/s, 40%

When the mean flow speed stayed at 20mm/s, the mock-sO$_2$ level was varied and imaged to show the performance of sO$_2$ estimation. Fig.4.4 shows the co-registered color Doppler and mock-sO$_2$ images at different sO$_2$ levels.
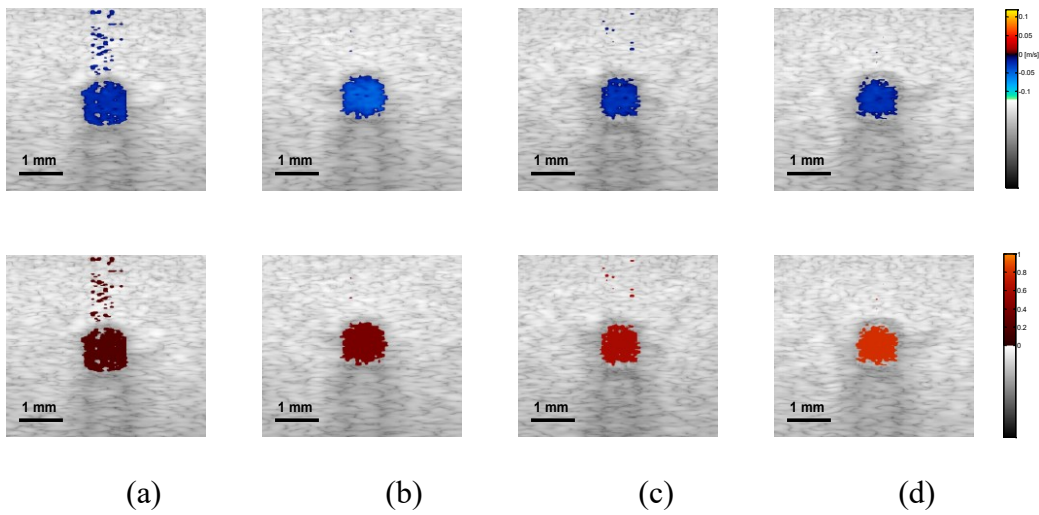
Fig.4.4 Co-registered color Doppler and mock-sO2 images of double-ink flow phantom: (a) 20mm/s, 20% (b) 20mm/s, 40% (c) 20mm/s, 60% (d) 20mm/s, 80%

4.3.2. Measurement Accuracy

Measurement accuracy can be elucidated by validating the mean of experimentally estimated quantities against known values. Mean flow speeds were quantified from color Doppler images (Fig.4.3) and plotted in Fig.4.5. Linear regression shows a good linear relationship between the measured and preset values with a correlation coefficient of $R^2 = 0.99$, a slope of 1.01 ± 0.03 (with 95% confidence bounds) and a zero-offset of -0.91 ± 1.38 mm/s.

We used black ink (Private Reserve Ink, IN) as a wavelength-independent optical absorber to calibrate for the influence of wavelength-dependent local optical fluence. This black ink was pumped through each vessel as a separate experiment, and multi-wavelength PA signals were acquired. Because light is completely absorbed within one acoustic resolution voxel at the surface of the black ink (regardless of wavelength), these PA signals were proportional to the local wavelength-dependent fluence and used to normalize the existing data for improved estimation of sO_2. Table.4.1 shows the mean values and standard errors of estimated mock-sO_2 before and after black ink correction. A Student's t-test was carried out to evaluate if the mean values of mock-sO_2 are significantly different from these two groups. Since the p-values are all within 0.05, the mean values of mock-sO_2 in these two groups are significantly different.
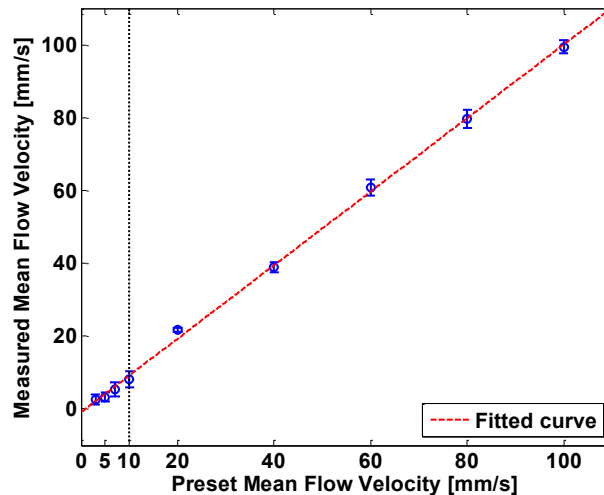
Fig.4.5 Measured mean flow speeds against preset values (double-ink flow phantom)

Table1. Mean values and standard deviations of mock-sO$_2$ of double-ink phantom with/without correction

Preset mock-sO$_2$ (%)	20	40	60	80
Measured mock-sO$_2$ (%)	18.8±0.8	37.0±1.1	56.3±1.1	72.3±1.4
Corrected mock-sO$_2$ (%)	20.3±0.8	39.7±1.2	59.8±1.2	74.4±1.3
Student's t-test p-value	0.03	0.02	0.02	0.03

Fig.4.6 shows the relation between measured and preset mock-sO$_2$ values. Linear regression indicates a good linear relationship with a correlation coefficient of R^2 = 0.99, a slope of 0.97±0.08 and a zero-offset of 0.01±0.04.
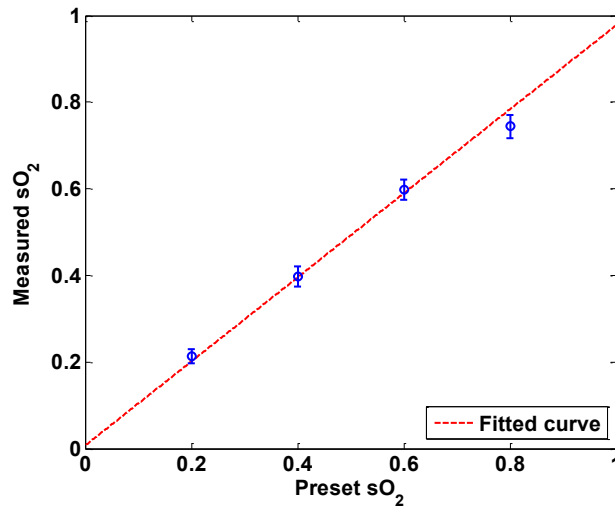
Fig.4.6 Measured mock-sO$_2$ against preset values (double-ink flow phantom)

4.3.3. *In vitro* phantom study of oxygen flux estimation

As illustrated in Fig.4.1, the fresh sheep blood with different sO$_2$ levels flows through the corresponding vessels embedded in tissue-mimicking base at different flow rates, and imaged by the combined system. Mean flow speeds were quantified from color Doppler images and plotted

against preset values (10mm/s, 20mm/s, 40mm/s, 60mm/s, 80mm/s) with linear least-square fitting in Fig.4.7. The correlation coefficient is 0.95 with a slope of 0.94±0.11 and a zero-offset of 2.98±3.93mm/s.
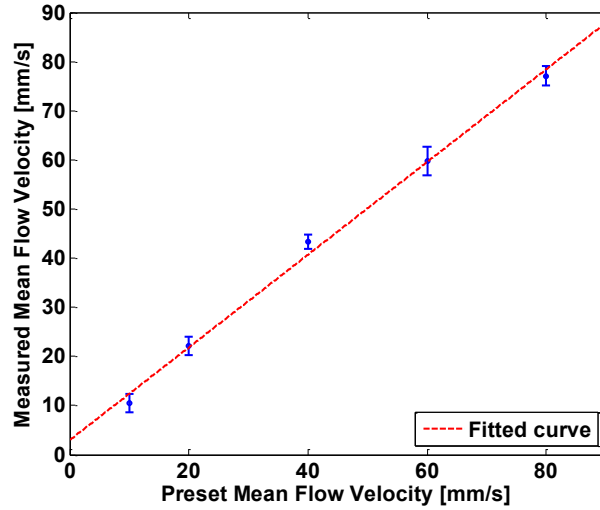
Fig.4.7 Measured mean flow speeds against preset values (sheep blood)

Four wavelengths (558nm, 564nm, 570nm and 576nm) are used to estimate sO_2. Since Hb and HbO_2 have the same optical absorption coefficient at isosbestic wavelength (570nm), the PA signal acquired at 570nm is proportional to C_{THb} regardless of the sO_2 level. In previous study [82], C_{THb} of the arterial sheep blood was measured to be 127g/L. We set this value as the C_{THb} of blood when quantifying oxygen flux. To determine the relative error in C_{THb} for Eq. (4.7), the amplitude of PA signals acquired at 570nm (from blood with varying sO_2 levels) was shown in Fig.4.8.
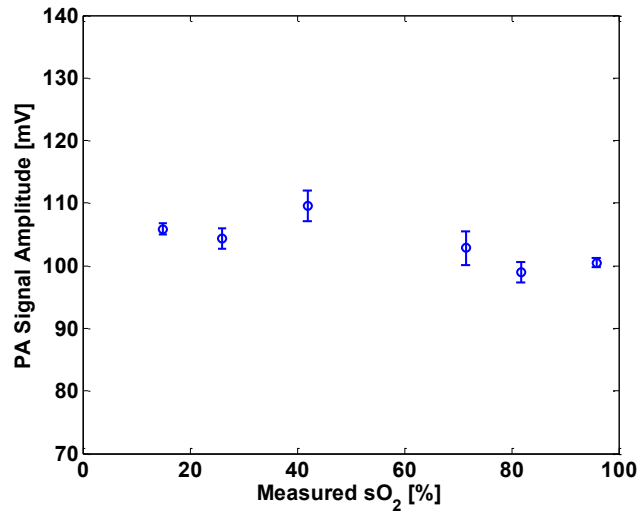
Fig.4.8 The amplitude of PA signals acquired at 570nm (blood with varying sO_2)

Both pO_2 and pH were measured simultaneously when the blood flow was imaged by the combined system. All the measurements were conducted under room temperature (T) of 23°C. Assuming that the CO_2 partial pressure $pCO_2 = 40mmHg$, the measured pO_2 values are calibrated to standard condition according to Eq. (4.9). To investigate the relationship between measured pO_2 and sO_2, we applied a least-square fitting of the measured pO_2 and sO_2 values to Eq. (4.8). Coefficients a_1 to a_7 in Eq. (4.8) are determined by fitting the paired values of sO_2 and pO_2.

As shown in Fig.4.9(a), our experimental results (red dash curve) agreed with the sigmoidal shape of Kelman's OHDC [81] with a correlation coefficient of 0.97. The Green curve is the simulated OHDC using coefficients reported in Kelman's experiments [85]. Our fitted curve (red dash curve) rises steeply with increasing pO_2 and reaches 90% sO_2 at pO_2 of ~40mmHg. In addition, the corresponding sO_2 was calculated from measured pO_2 according to Eq. (4.9). Fig.4.9(b) shows the relation between the sO_2 measured by PA method and calculated from measured pO_2. Linear regression shows that the correlation coefficient is 0.92 with a slope of 1.11±0.10 and a zero-offset of -0.07±0.07.

From measurements of all these parameters, blood oxygen flux of a single vessel was estimated by Eq. (4.5) at different flow velocities and sO_2 levels, and the uncertainty was quantified by Eq. (4.7). Results are shown in Fig.4.10. The unit of estimated oxygen flux is ml/min. The mean standard error is 0.1 ml/min.

(a)   (b)
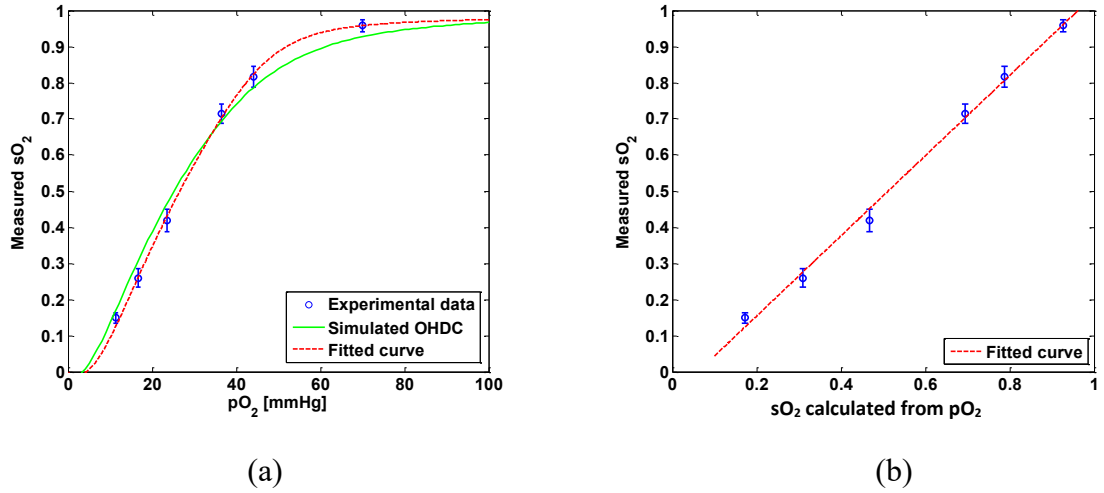
Fig.4.9 (a) The relationship between measured pO2 and measured sO2 (b) The linear least-square

fitting of the measured sO2 and sO2 calculated from pO2
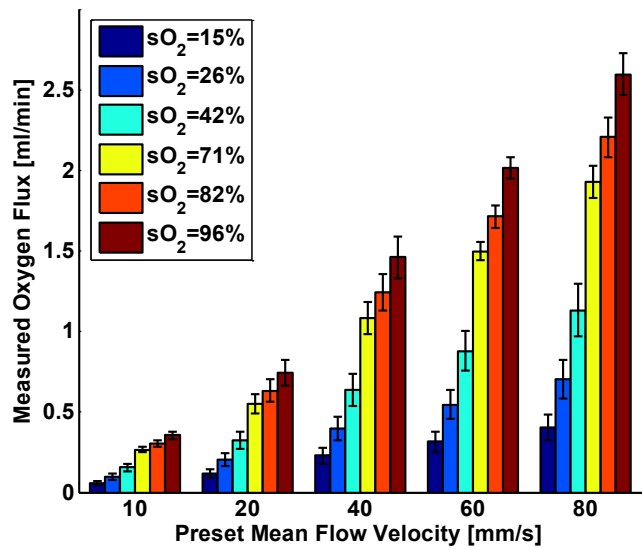
Fig.4.10 Blood oxygen flux [ml/min] at various sO2 levels and mean flow speeds

4.4. Discussion

We have demonstrated for the first time a photoacoustic and ultrasound method for imaging local blood oxygen flux in single vessel. Our combined photoacoustic and high-frequency ultrasound microscopy system shows good performance on both flow velocity and sO_2 estimation at penetration depths >2-3mm. For the task of cross-sectional area estimation, a circular region is selected so that all the color pixels in the power Doppler image can be fitted into the circle. For different vessel sizes and flow speeds, it may be possible to improve our estimation of fractional blood volume by careful selection of photoacoustic or power Doppler parameters. On the other hand, color Doppler velocity estimation may be improved by only computing Doppler estimates in locations where photoacoustic or power Doppler signals exist.

One long term goal of our research is to use this system to estimate MRO_2 *in vivo*. As shown in Eq. (4.1), the sub-surface optical fluence is often unknown in photoacoustic imaging so that quantitative estimation of oxygen saturation is challenging for animal models. In this work, we used a black ink correction method to reduce the influence of wave-independence of the local optical fluence. In future studies, we would like to couple PAM with a technique termed oblique incidence reflectometry which can provide a good first-order estimate of local optical fluence to improve our sO_2 estimation. This proposed method will require validation. Even if accurate fluence correction is not possible, relative changes of oxygen flux into and out of a given region, and within a given range of imaging depths may prove informative if not absolutely quantitative.

Moreover, the challenge of imaging depth and reduced imaging speed may be limitations of the high-frequency swept-scan system. A clinical array system may be incorporated to allow images at multi-cm depths and higher frame rates. Work in progress includes implementing the photoacoustic and Doppler ultrasound method for MRO_2 estimation on a clinical array system.

4.5. Conclusion

We have developed a combined photoacoustic and high-frequency ultrasound imaging system with a 25MHz single element transducer and confocal dark-field laser illumination optics. Flow phantoms are constructed to validate the color flow estimation and multi-wavelength sO_2 estimation. *In vitro* sheep blood phantom experiments have been performed at different sO_2 levels and mean flow speeds. We also experimentally demonstrate for the first time the feasibility of

imaging local blood oxygen flux of a single vessel by combining photoacoustic oximetry and color Doppler ultrasound. Uncertainties at all experimental conditions are quantified to show a good performance of blood oxygen flux estimation. The mean standard error is 0.1ml/min, which means that we can distinguish oxygen fluxes that differ by this amount.

5. Estimation of Cerebral Metabolic Rate of Oxygen Consumption using Combined Multi-Wavelength Photoacoustic Microscopy and Doppler Micro-Ultrasound

5.1. Introduction

The brain is one of the most energy-demanding and metabolically active organs of the body. Although it comprises only 2% of body weight, it receives about 15% of cardiac output and uses 20% of total body oxygen and 25% of total body glucose [5]. Under normal physiological conditions, oxidative metabolism of glucose is the primary way to produce adenosine triphosphate (ATP), the most important energy source for the brain. Oxygen needs to be delivered to the cerebral tissue at a rate that is biochemically-appropriate to neurons' metabolic needs [5]. The cerebral metabolic rate of oxygen consumption ($CMRO_2$) depends on the density of neurons, and on their state of functional activation [83]. Many of the common disorders of the brain, such as Alzheimer's, Parkinson's, Huntington's, and others have been found to be associated with alterations in the cerebral oxygen metabolism [6] [7]. Therefore, the measure of $CMRO_2$ would not only enable a better understanding of the normal physiology during rest, sleep, anesthesia, aging or functional brain task [10] [84], but also be important for research and clinical applications related to brain disorders, stroke, and help to improve the management of patients who are at the risk of developing brain hypoxia-ischemia [12] [85].

Since the extraction of oxygen from cerebral tissue is closely matched to the brain's metabolic needs [83], $CMRO_2$ should be equal to the total amount of oxygen delivered to the cerebral tissue per unit time minus the amount leaving in the venous circulation per unit time . As shown in Eq.(5.1), the cerebral blood flow (CBF) and the arteriovenous oxygen difference ($AVDO_2$) are the key parameters to estimate $CMRO_2$ based on Fick's principle [86]. Under steady state physiologic conditions, $CMRO_2$ remains relatively constant over a range of arterial partial pressure of oxygen

(PaO2), typically 23-100mmHg, due to the cerebral autoregulation mechanism [83]. During mild hypoxia (PaO2 < 90mmHg) , the oxygen supply may be inadequate, however, metabolic demand may still be met by elevated CBF or reduced venous blood saturation, which means the higher extraction of oxygen from the blood [87]. Severe hypoxia (PaO2 < 30mmHg) may cause significant decrease in CMRO2 due to insufficient blood flow or oxygen extraction compensation [88]. The metabolic autoregulation is a negative feedback system that seeks to balance the oxygen supply to its demand in a certain range [89].

$$CMRO_2 = CBF \times AVDO_2 \tag{5.1}$$

Currently, techniques to obtain CMRO2 are limited. The important criteria for such techniques include noninvasiveness, adequate spatial and temporal resolution, low radiation exposure, good safety profile, and widespread clinical availability [18]. Unfortunately, no *in vivo* method can fulfill all of these requirements. In early studies, the jugular vein oximetry involving catheterization has been used for a surrogate measure of CMRO2 but is invasive [19]. Positron Emission Tomography (PET) with ^{15}O-labled radiotracers provides the most direct measurement of CMRO2 [20]. Yet, the spatial resolution is poor (~1cm for clinical system) and the high ionizing radiation dose prevents its repeated use on the same patient. Magnetic Resonance Imaging (MRI) is also applied to image CMRO2 by utilizing the Blood Oxygenation-Level Dependent (BOLD) effect. BOLD MRI is noninvasive and can be performed with high spatial resolution, but it is only sensitive to deoxy-hemoglobin and has trouble distinguishing between changes in oxygen saturation and blood flow [21]. In recent studies, phase-contrast MRI has been proposed to quantify the blood flow in major inflow vessels, however, for the oxygen saturation estimation only large-sized vein (superior sagittal sinus) can be targeted [35]. Moreover, the complex setup and high expenses preclude PET and MRI for many bedside clinical applications.

Imaging techniques based on optical contrast, which is sensitive to blood functional parameters, have been widely employed for the assessment of tissue oxygen metabolism. Near-Infrared Spectroscopy (NIRS) offers a means to estimate CMRO2 noninvasively with the blood flow information provided by diffuse correlation spectroscopy (DCS) [22] [23]. The main drawback is that the spatial resolution is relatively low due to strong optical scattering. Photoacoustic imaging overcomes this limitation by ultrasonically imaging optical contrast through the photoacoustic effect [17]. Optical-resolution photoacoustic microscopy (OR-PAM) has been used to estimate

oxygen consumption in superficial tissues [24]. This technique utilizes fine optical focusing to achieve high lateral resolution (~5μm), however, the imaging depth is shallow (<1mm) and the detectable flow speed (<12mm/s) is limited due to low laser repetition rate [25]. While recent work suggests hope for photoacoustic flow estimation in deep tissues (>1mm) using acoustic-resolution photoacoustic imaging [26], it is less established than Doppler ultrasound methods we selected in this paper.

Here we propose $CMRO_2$ estimation using photoacoustic and Doppler ultrasound methods. The combination of local blood oxygenation estimation and flow estimation in deep vessels is accomplished with a custom photoacoustic and micro-ultrasound scanning system. We previously demonstrated oxygen flux estimation in a phantom study using such a system [90]. In this paper, the $CMRO_2$ is estimated *in vivo* by combining the measurements of arterial and venous oxygen saturation, and flow rate of internal jugular vein.

5.2. Methods

5.2.1. Experiment Setup

Our custom photoacoustic and micro-ultrasound system was constructed by a combined light delivery and ultrasound probe, a tunable laser, and a computer-controlled scanning, triggering and data acquisition system. As the irradiation source, a tunable optical parametric oscillator (Surelite OPO Plus, Continuum, California) was pumped by a Q-switch Nd:YAG nanosecond-pulsed laser (Surelite III, Continuum, California) at a repetition rate of 10Hz. The tuning range is from 410nm to 710nm. The laser output was coupled into a bifurcated fiber-bundle light guide with a core diameter of 185μm (900 fibres, CeramOptec Industries, Germany). An acrylic probe was designed to position the bifurcations of the light guide around a 25MHz single element focused ultrasound transducer (V324-SM, Olympus Panametrics-NDT, Massachusetts). The transducer was placed such that the focus of the transducer and the center of the illumination spot (~1cm^2) were aligned. The illumination fluence was measured about 10mJ/cm^2. This probe was mounted on a 3-axis motion system for B-scan and C-scan imaging. A PCI motion card (NI7350, National Instruments Inc., Texas) was used to control a high-precision 3-axis motion stage with three integrated stepper motors (23Y002D-LW8, Anaheim Automation, California). Fast-scanning was accomplished with

a voice-coil actuator as previously described [80] [79] while vertical and elevational translation was accomplished using the stepper-motors.

Signals from the transducer were amplified by a variable-gain pre-amplifier then further amplified by an ultrasound pulser/receiver (5073PR, Panametrics-NDT, Massachusetts). The variable gain stage (AD603ARZ evaluation board, Analog Devices, Massachusetts) was used to implement time-gain compensation (TGC). The TGC curves in a range of 40dB for both ultrasound and photoacoustic imaging were controlled via a digital input-output (DIO) card (NI PCI-6542, National Instruments Inc., Texas). Signals were digitized using a multi-channel data acquisition card (CS8289 Gage Cobra, Gage Applied Systems Inc., Illinois) with 12-bit dynamic range and sampling rates as high as 125MSamples/s, and post-processed using MATLAB (R2012a, MathWorks, Massachusetts).
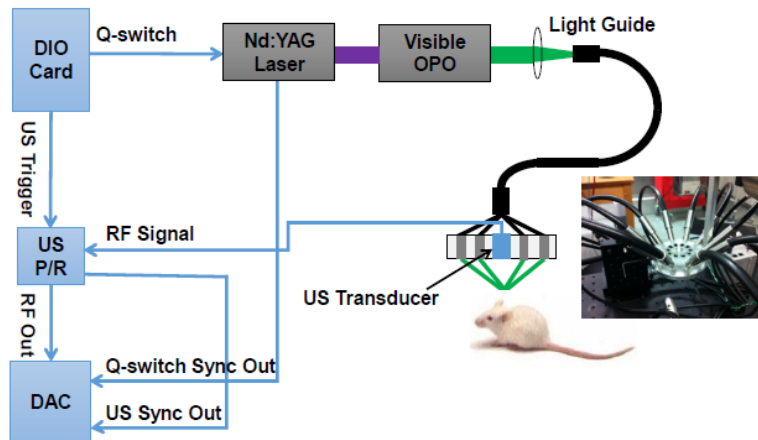
Fig.5.1 A schematic of light delivery and data acquisition setup and photograph of the fiber bundle delivery surrounding the transducer. (DIO: Digital Input Output, US: Ultrasound, P/R: Pulser/Receiver, DAC: Data Acquisition Card)

Our system provided combined photoacoustic and Doppler ultrasound mode. Details are referred to our previous work [79]. In brief, a pulse sequence was generated by the DIO card and sent to interleave laser and ultrasound triggers. Photoacoustic and Doppler ultrasound images were co-registered after signal processing. A schematic of the constructed system is illustrated in Fig.5.1, which also shows a photograph of the probe with bifurcated fiber-bundle light delivery.

5.2.2. Animal preparations

Sprague Dawley rats (Charles River Breeding Laboratories, Massachusetts), female, weighing about 50g, were employed in this study. Each rat was first anesthetized in an induction chamber with 1.25%-1.5% (volume to volume) vaporized isoflurane (IsoFlo, Zoetis Inc., New Jersey). After the rat was anesthetized, it was immobilized on a customized animal holder and fitted with a nose breather. The inhaled gas was controlled by an animal anesthesia system (EZ-SA800 Single Animal System, E-Z Anesthesia, Philadelphia) mixing 1% vaporized isoflurane with certain ratios of oxygen and nitrogen. Body temperature was maintained at 37ºC with a temperature-controlled heating pad, and the blood oxygenation levels and heart rates were monitored by a pulse oximeter (Nonin 8600V, Nonin Medical Inc., Minnesota) clamping on the hind leg of the animal. All *in vivo* procedures and protocols were reviewed and approved by University of Alberta Animal Care and Use Committees.

The physiological conditions (hyperoxia, normoxia and hypoxia) of the animal can be achieved by varying the fraction of inspired oxygen (FiO_2), which alters the arterial oxygen saturation acutely [88]. In this study, mild hypoxia and mild hyperoxia (PaO_2 within the range of 30-100mmHg) were introduced to avoid significant changes in cerebral oxygen consumption. According to Kelman's OHDC [81], the arterial oxygen saturation should be within the range of 60%-100%. The animal was exposed to different FiO_2 during gas anesthesia by mixing the output of regulated oxygen and nitrogen tanks with precise flow measurements read from the respective flow meters on the tanks. The global arterial oxygen saturation was recorded at each FiO_2.

5.2.3. Blood flow estimation using Doppler bandwidth broadening

Phantom imaging studies of flow estimation using double-dye mixtures and sheep blood were previously reported [90]. Pulsed color Doppler ultrasound was used for flow velocity estimation. A sequence of modulated ultrasound pulses was transmitted along a certain Doppler angle, and the flow velocities were calculated from detected phase shifts in received echoes [27]. However, when the Doppler angle approaches 90º, the phase shift almost vanishes, and the transverse flow velocity cannot be identified. In phantom studies [90], the appropriate Doppler angle was possible owing to oblique vessel orientation, however, the *in vivo* measurements were to be done along vessels almost perpendicular to the ultrasound beam axis. Considering the difficulty of creating such a

Doppler angle with our wide-footprint probe, we adopted a different approach termed Doppler bandwidth broadening to transverse flow estimation, similar to that used in previous ultrasound and OR-PAM techniques [25] [51]. In brief, assuming negligible velocity variation within the sample volume and sufficient velocity resolution, the bandwidth of the Doppler spectral broadening is given as

$$B_w = \frac{2f_0}{c_0}\frac{D}{F}v\sin\theta, \tag{5.2}$$

where B_w is the Doppler bandwidth, f_0 is the center frequency, c_0 is the speed of sound, D is the transducer aperture, F is the focal length, v is the flow velocity, and θ is the Doppler angle of the flow relative to the ultrasound beam axis. Since the square of Doppler bandwidth B_w can be approximated by the variance of the Doppler spectrum [51], the transverse flow can be estimated as

$$v_\parallel = \frac{c_0}{2f_0}\frac{F}{D}\sqrt{\sigma^2}, \tag{5.3}$$

where σ^2 is the variance of Doppler spectrum, which is calculated routinely in correlation-based color Doppler ultrasound algorithm [27].

Our system also provided power Doppler ultrasound to image blood volume fractions. Different from flow velocity estimation, the intensity of power Doppler image is proportional to the number of scatterers moving within a vascular volume rather than the frequency shifts they generate [52], which makes it more sensitive to blood flow detection and independent of Doppler angles [78]. Since tissues surrounding blood vessels often generate much stronger scattered signals than moving blood, clutter filtering is necessary before velocity estimation and power calculations. Here an eigen-filter was designed and implemented based on the statistics of the clutter and tissue movement. The correlation matrix of the received signals was decomposed into eigenvectors and eigenvalues by the discrete Karhunen-Loeve transform (DKLT), and then eigenvalues were sorted in decreasing amplitude. Since the eigenvalue spectrum represents the power distribution of the frequency components [57], and the power of clutter signals arising from tissues is much higher than other components, the clutter space and flow space can be partitioned in the spectrum. Appropriate filter order was determined experimentally to give the best trade-off between clutter rejection and preservation of flow. Details refer to Section 2.2.7.

5.2.4. Oxygen saturation estimation using photoacoustic methods

Blood oxygen saturation (sO_2) estimation was validated in phantom studies [90] by relating photoacoustic estimates of sO_2 to sO_2 levels measured from knowledge of measured pO_2 and pH and given known oxygen dissociation curves. As this is significantly more challenging *in vivo*, in this paper we chose to implement two independent photoacoustic methods to cross-validate sO_2 estimates. The first, and most traditional approach was to solve for unknown concentration of oxy-hemoglobin and concentration of deoxy-hemoglobin, given measured photoacoustic signals and known molar extinction coefficients. Details are referred to Section 2.3.3.

This approach suffers from unknown wavelength-dependent fluence which is often assumed a constant or requires wavelength-dependent calibration. A second approach proposed in [70] is to use multi-wavelength photoacoustic measurements at different oxygen saturation levels and solve a system of equations to estimate the different sO_2 levels. Details are referred to Section 2.3.3. This approach requires no wavelength-dependent fluence calibration factor but assumes that the optical properties of tissue between the vessels of investigation and the tissue surface do not change their optical properties. Thus, neither approach is devoid of approximations, yet consistency in estimates would provide cross-substantiation.

5.2.5. Cerebral metabolic rate of oxygen consumption (CMRO₂) estimation

According to Eq.(5.1), assuming that CBF is the only way of oxygen delivery to the brain, the global CMRO$_2$ can be estimated by combining the measurements of CBF, arterial oxygen saturation ($sO_{2,a}$) and venous oxygen saturation ($sO_{2,v}$),

$$CMRO_2 = CBF \times C_{THb} \times \zeta \times (sO_{2,a} - sO_{2,v})/w, \tag{5.4}$$

where C_{THb} is the total concentration of hemoglobin with a unit of g/ml, ζ is the oxygen-carrying capacity of 1.39ml oxygen per gram of hemoglobin on the basis of a typical C_{THb} level (0.147g/ml at a hematocrit of 0.42) [91], and w is the weight of the weight of the brain. Based on anatomic and hemodynamic studies, oxygen is supplied to the brain by four feeding vessels: the left and right internal carotid arteries and the left and right vertebral arteries. Although the contribution of each artery to the total cerebral perfusion is different, the oxygen saturation levels in these vessels are comparable to each other. For the blood draining from the brain, the pair of internal jugular

veins provide the majority (~80%) of the venous drainage via deep veins and dual sinuses. In our *in vivo* study, the combined imaging system scanned across the neck of the subject, and the $sO_{2,a}$ and $sO_{2,v}$ were estimated from the carotid artery and jugular vein in the field of view (FOV). For CBF estimation, we used flow rates of internal jugular veins by measuring the cross-sectional area ($\overline{A}_{IJV}$) and the mean flow velocity ($\overline{v}_{IJV}$) of the vessel. Thus, the representative $CMRO_2$ can be expressed as

$$CMRO_2 = CBF \times \overline{A}_{IJV} \times \overline{v}_{IJV} \times C_{THb} \times \zeta \times (sO_{2,a} - sO_{2,v})/w, \qquad (5.5)$$

5.3. Results

First, the bandwidth broadening Doppler ultrasound approach was validated in phantoms with embedded tubing by comparing estimated flow velocity against pre-set flow speeds, as shown in Fig.5.2. The construction of the cornstarch-gelatin phantom can be referred to our previous work [90]. Under the assumption of fully-developed parabolic flow, we observed excellent consistency and sensitivity to flow velocities of several mm/s, sufficient for *in vivo* flow estimation in murine carotid artery and jugular veins. The correlation of determination R^2 of linear least-square fitting is 0.99 with a slope of 0.94 and a zero-offset of 4.2 mm/s.
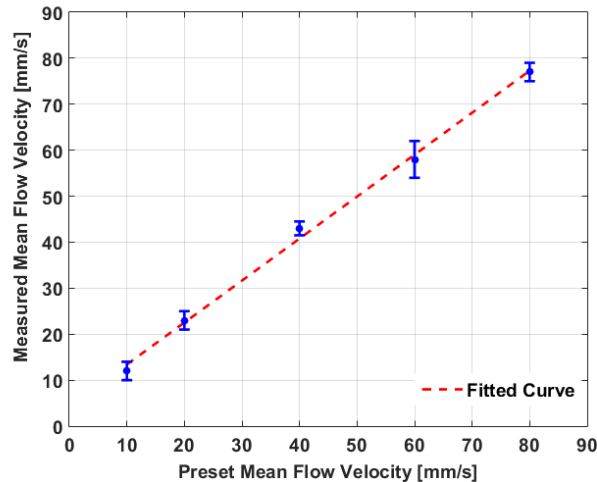
Fig.5.2 Comparison between the pre-set and the measured flow velocity of phantom using Doppler bandwidth broadening

Next, we estimated $CMRO_2$ *in vivo* using Doppler ultrasound for flow estimation and multi-wavelength photoacoustic methods for sO_2 estimation. The animal was prepared as described in

Section 5.2.2 and scanned across the neck at the speed of 5mm/s under different physiological conditions. The global arterial sO_2 was recorded by the pulse oximeter during the modulation of FiO_2. Fig.5.3 shows representative *in vivo* co-registered photoacoustic (acquired at 580nm), Doppler bandwidth broadening and power Doppler images of the carotid artery and jugular vein when global arterial sO_2 was measured at 85%. The artery was located >2mm in depth, and the vein was located ~1mm under the skin. As in Fig.5.3 (b), the mean flow speed was quantified as 146mm/s. For the task of cross-sectional area estimation, a circular region was selected so that all the color pixels in the power Doppler image (Fig.5.3(c)) were fitted into the circle.
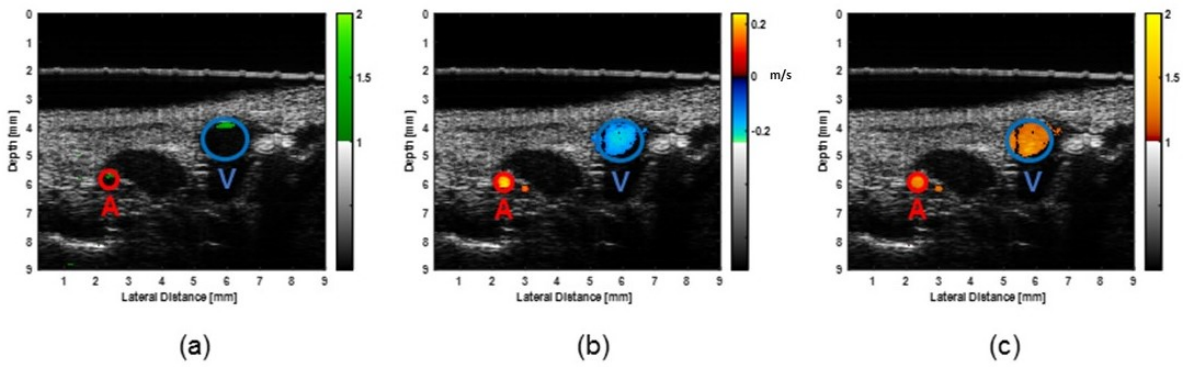
Fig.5.3 Representative *in vivo* co-registered images of carotid artery (labeled as "A") and jugular vein (labeled as "V"): (a) photoacoustic image acquired at 580nm, (b) Doppler bandwidth broadening image, the color bar shows the absolute value of flow speed and direction, (c) power Doppler image

Fig.5.4 shows the measured venous mean flow velocities as a function of global arterial sO_2 measured by the pulse oximeter. The appropriate ultrasound pulse-repetition-rate was chosen to ensure that the flow speeds were within the detectable range [38]. The mean flow velocity of the internal jugular vein begins to drop above a global arterial sO_2 of ~85%.
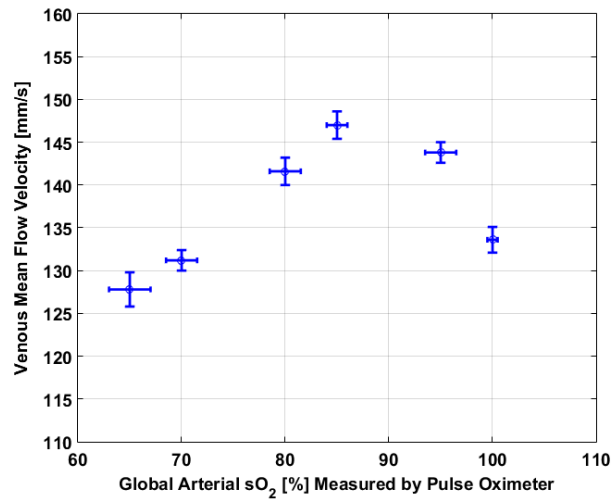
Fig.5.4 Venous mean flow velocities measured from hyperoxia (global arterial sO$_2$ ~100%) to hypoxia (global arterial sO$_2$ ~65%) conditions

Fig.5.5 shows photoacoustic sO$_2$ estimates in both arteries and veins as a function of measured global arterial sO$_2$ from a pulse oximeter. As described in Section 5.2.4, we used two photoacoustic methods to cross-validate our sO$_2$ estimation. Method 1 is the traditional approach which solves for unknown concentrations of oxy- and deoxy- hemoglobin using measured photoacoustic signals and known molar extinction coefficients, while method 2 uses multi-wavelength photoacoustic measurements at different sO$_2$ levels to solve a system of equations to estimate the different sO$_2$ levels. Fig.5.5 shows the comparison of arterial sO$_2$ estimations between method 1 and method 2. The estimates are consistent with p<0.05. It can also be observed that the sO$_2$ estimates from arteries are close to the pulse oximeter values. The consistency ensures the validation of sO$_2$ estimation in arteries and offers confidence in sO$_2$ estimation in veins.
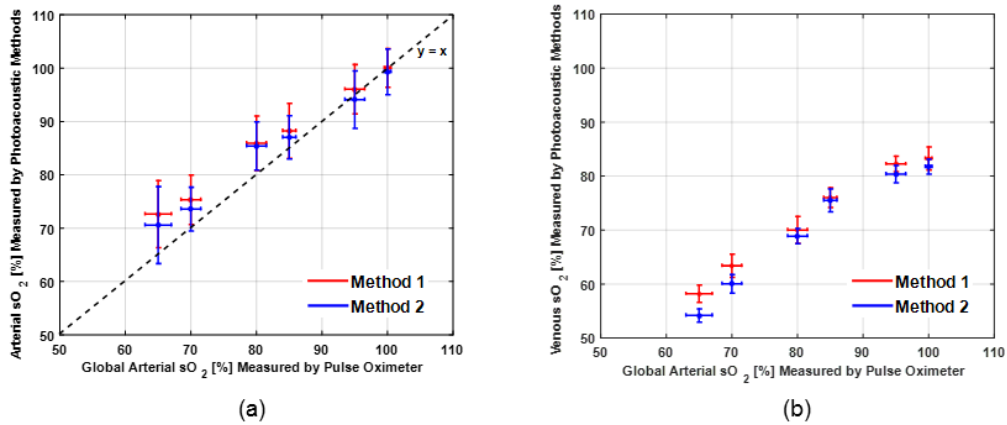
Fig.5.5 Comparison of photoacoustic sO$_2$ estimations between Method 1 and Method 2 in (a) carotid artery and (b) jugular vein. The arterial sO$_2$ error bars are larger than venous sO$_2$ error bars, likely due to flow pulsatility in arteries.

The representative CMRO$_2$ were quantified according to Eq.(5.5) in Section 5.2.5. Here we used a typical C_{THb} level of 0.147g/ml at a hematocrit of 0.42 [91]. The results are shown in Fig.5.6 as a function of global arterial sO$_2$ as measured using pulse oximetry. As anticipated, the CMRO$_2$ remains relatively constant during mild hypoxia and hyperoxia (global arterial sO$_2$ of 65%-100%), consistent with the hypothesis of brain metabolic autoregulation.
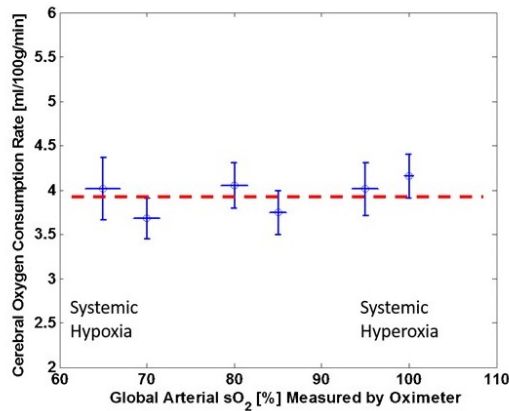
Fig.5.6 The estimated representative CMRO$_2$ (ml/100g/min) as a function of varying global arterial sO$_2$ measured using pulse oximetry during modulation of FiO$_2$ under anesthesia. Error bars are standard deviations estimated according to the theory of propagation of errors.

5.4. Discussion

Given the major significance of oxygen metabolism in health and disease, our work represents a novel approach to measure this metric using photoacoustic and ultrasound technologies. Current efforts use high-frequency ultrasound and visible light for animal models owing to limited penetration requirements. It should be noted, however, that depths investigated represent unreachable penetrations for previous oxygen metabolism progress using OR-PAM.

In this study, the total CBF is quantified by measuring outflow instead of inflow [92], as internal jugular veins provide the majority (~80%) of the venous drainage from the brain. Since not all the blood vessels are counted for the measurements, the $CMRO_2$ we measure is only a representative measure of oxygen consumption. Given the bifurcation of the common carotid artery into internal and external our estimate of $CMRO_2$ may be influenced by including facial oxygen flux. Encouragingly, the representative $CMRO_2$ remains relatively constant during the modulation of the fraction of inspired oxygen (FiO_2), which agrees with the hypothesis of cerebral metabolic autoregulation in the range of 23-100mmHg of PaO_2. During mild hypoxia, the metabolic demand may be met by elevated CBF or higher extraction of oxygen from the blood [87]. We have observed that the mean flow speed of internal jugular vein was dropping at global arterial sO_2 of ~85%. This may be the consequence of vasodilation, which helps to increase the cerebral blood volume under the hypoxia condition [83].

Uncertainty due to measurement variability are quantified by measuring sO_2 and flow rates at least 3 times and estimating standard deviations. Future work should aim to reduce uncertainties by optimization of light fluence, using higher-sensitivity detectors, and by a potential combination of motion compensation and judicious averaging. Array transducers may improve frame-rates to real-time if sufficient wavelength-switching capabilities are available, whereas current ultrasound B-scan speeds are limited to ~15fps while photoacoustic B-scans are limited by the 10Hz repetition rate of the laser to acquire a single A-scan.

Future work should investigate conditions where brain autoregulation is impacted such as stroke, trauma, acute sepsis, brain damage, and potentially neurodegenerative conditions. Pre-clinical investigation with animal models may offer invaluable insight prior to human translation. Human translation may be possible with infrared light and diagnostic-frequency transducers, especially in

infants and children, considering the superficial depths of internal carotid and jugular vessels in these subjects.

5.5. Conclusion

We have demonstrated *in vivo* estimation of cerebral metabolic rate of oxygen metabolism in murine models using a custom combined photoacoustic and micro-ultrasound system. Estimates of CMRO$_2$ are based on arterial and venous oxygen saturation measurements using photoacoustic methods, and flow measurements based on Doppler ultrasound. Photoacoustic estimates of oxygen saturation in arteries is validated with pulse oximetry while venous sO$_2$ is cross-validated using two independent photoacoustic methods. The estimated CMRO$_2$ remains relatively constant from mild hypoxia to mild hyperoxia conditions, which agrees with the hypothesis of cerebral metabolic autoregulation. The demonstrated method for estimating oxygen consumption may have significant applicability in other tissues and has potential for clinical translation owing to its label free nature.

6. Conclusion and Future Work

6.1. Work done in this dissertation

The work presented in this dissertation contributes to the long-term vision of developing a multi-modality imaging technique for non-invasive *in vivo* estimation of metabolic rate of tissue oxygen consumption (MRO$_2$). Since photoacoustic imaging is well suited for functional imaging of blood oxygenation parameters with high spatial resolution and high optical contrast, and Doppler ultrasound is capable of imaging a wide range of flow velocities, we proposed to combine and take advantage of both modalities to better visualize and estimate MRO$_2$. Contributions in this dissertation can be described in three sections.

6.1.1. Comparative study on blood volume detection

- We pioneered to develop a combined photoacoustic and high-frequency power Doppler ultrasound imaging system for the first time by using a swept-scan 25MHz ultrasound transducer with confocal dark field laser illumination optics. Photoacoustic and power Doppler ultrasound images are generated and co-registered after signal processing. This combined

system aims to take advantage of both modalities to improve blood volume detection, which is important for flow estimation when quantifying MRO$_2$.

- By using our combined imaging system, we first presented a quantitative and objective comparison on blood volume detection using flow phantoms with various combinations of vessel size (with inner diameter of 0.2mm and 0.86mm), flow velocity (1mm/s and 5mm/s), and optical wavelength (532nm and 630nm). The selection of vessel sizes and flow velocities is a representative of venules and arterioles, or small vessels in microcirculation. Receiver operating characteristic (ROC) analysis was used to objectively quantify the performance of both power Doppler and photoacoustic modes for the task of blood volume detection. This study highlights relative merits and shortcomings of these two imaging modalities, gives further guidance on fractional blood volume estimations *in vivo* under different circumstances.

6.1.2. Phantom validation on blood oxygen flux estimation

- We further upgraded our combined system to add capabilities of multi-wavelength photoacoustic imaging and color Doppler ultrasound, aiming to take advantage of both modalities to better estimate MRO$_2$. Since the mean flow velocity can be estimated using color Doppler ultrasound, vessel cross-sectional area can be quantified from power Doppler or photoacoustic images, oxygen saturation of hemoglobin (sO$_2$) and total concentration of hemoglobin (C$_{THb}$) can be estimated using multi-wavelength photoacoustic methods, our system is able to provide all of the parameters necessary for MRO$_2$ estimation.

- We experimentally demonstrated for the first time the feasibility to image local oxygen flux of a single vessel using our combined system. Double-ink phantom studies first validated and determined the accuracy of flow velocity and mock-sO$_2$ estimation. *In vitro* phantom experiments using freshly collected sheep blood then demonstrated the capability of imaging blood oxygen flux in a single vessel at various sO$_2$ and flow velocity combinations. Both sO$_2$ and partial pressure of oxygen (pO$_2$) were measured simultaneously and fitted into the oxy-hemoglobin dissociation curve (OHDC). Blood oxygen flux was estimated from measurements of all key parameters, and the uncertainty of the estimate was quantified. This work is important for our next step towards *in vivo* MRO$_2$ estimation.

6.1.3. *In vivo* cerebral oxygen consumption estimation

- By using our combined photoacoustic and Doppler ultrasound system, we first demonstrated and reported the cerebral MRO$_2$ estimation *in vivo* by combing the measurements of arterial and venous sO$_2$, and flow rate of internal jugular vein on a Sprague Dawley rat model.

- Some modifications have been made to adapt our system for complex *in vivo* circumstances. The light delivery probe was re-designed to deliver more optical energy to the tissue beyond 2mm. Doppler bandwidth broadening technique was introduced to estimate transverse flow velocity due to the vanishing of Doppler angles for *in vivo* measurements. Also, since it was scientifically more challenging for sO$_2$ estimation *in vivo*, we implemented two independent photoacoustic methods for a cross-validation.

- Physiological conditions of the animal was controlled from mild hypoxia to mild hyperoxia, and cerebral MRO$_2$ was estimated under different conditions. Estimates of cerebral MRO$_2$ under different physiological conditions were based on arterial and venous sO$_2$ measurements using photoacoustic methods, and flow measurements of internal jugular vein using Doppler bandwidth broadening. The results have shown that the cerebral MRO$_2$ remains relatively constant from mild hypoxia to mild hyperoxia, which agrees with the hypothesis of brain metabolic auto-regulation mechanism.

- This multi-modality imaging technique for MRO$_2$ estimation is non-invasive, less expensive, potentially applicable to other tissues and clinical translation owing to its label free nature.

6.2. Limitations and future work

Although we have demonstrated the capability of imaging MRO$_2$ in a pre-clinical animal model using our combined photoacoustic and high-frequency Doppler ultrasound system, some limitations and potential issues should be addressed for further development. High-frequency ultrasound provides high spatial resolution, however, the imaging depth is limited due to high attenuation. The frequency dependency of ultrasonic attenuation can be represented by the expression $\mu = af^b$, where μ is the ultrasonic attenuation coefficient, a and b are constants, and f is the frequency of ultrasound [38]. The attenuation increases with the frequency and the penetration depth decreases with the frequency. Therefore high-frequency imaging yields improved spatial resolution at the expense of a shallower imaging depth. Moreover, although

mechanically scanned single element transducer is cost-effective, the mechanical motion of the transducer limits the frame-rate. For example, frequency between 30 to 60 MHz yields a frame-rate of 30 frames/second or even lower, which is not adequate to image the hearts of small animals [93]. In future studies, a clinical array system may be incorporated to allow images at multi-centimeter depths based on clinical applications. With the development of array transducer, high-frequency linear arrays in the 20-50 MHz range could be used to alleviate the problem of reduced frame-rate, and even realize real-time imaging if sufficient laser pulse repetition rate and wavelength switching capability are available.

Another limitation is the unknown local optical fluence. Based on photoacoustic effect, photoacoustic signal directly measures specific optical absorption, which is the product of the tissue-intrinsic optical absorption coefficient and the local optical fluence. Therefore, absolute oxygen saturation quantification requires knowledge of the local optical fluence. In our phantom studies, we used black dye experiments to calibrate local fluence. However, due to the optical heterogeneities in tissue, calibration of local fluence *in vivo* is challenging. In pre-clinical and clinical studies, this can be achieved through invasive measurements or sophisticated modeling of light transportation [94]. Non-calibration method is also proposed based on the assumption of local fluence does not change if the sO_2 variation is small and localized, i.e. within the blood vessel or a tumor region [70]. Therefore, future work should also aim to reduce uncertainties by optimization of light fluence calibration.

Other future work directions also include higher-sensitivity detectors, a potential combination of motion compensation and judicious averaging, better wall-filtering, and three-dimensional visualization.

6.3. Conclusion and possible applications

In the first chapter of this dissertation, we proposed a combined photoacoustic and Doppler ultrasound technique for MRO_2 estimation. To achieve this goal, we have developed a combined multi-wavelength photoacoustic and high-frequency (25MHz) Doppler ultrasound imaging system, and successfully demonstrated the capability of using this system to estimate cerebral MRO_2 in a pre-clinical animal model. This technique is completely non-invasive, with no exposure to ionizing radiation, and could be inexpensive to be used in research labs or medical clinics. The

high spatial resolution, high sensitivity in blood oxygenation, and capability of imaging flow velocities and dynamics, make this technique suitable for many research and clinical applications related to MRO_2 estimation.

In Chapter.5, we have demonstrated the feasibility of monitoring cerebral MRO_2 in a pre-clinical animal model. Human translation may be possible with infrared light and diagnostic-frequency transducers, especially in infants and children. Possible applications include the study of brain auto-regulation mechanism and investigation of conditions where brain auto-regulation is impacted such as stroke, trauma, acute sepsis, brain damage, and potentially neurodegenerative.

In neonates, cerebral oxygen metabolism is thought to play a particularly critical role in the early brain development after birth. An accurate estimate of cerebral MRO_2 could not only help to diagnose brain injuries, such as hypoxic-ischemic encephalopathy, stroke and metabolic disorders that may lead to long-term neurologic deficits, but also provide an insight into therapeutic response during hypothermia neuroprotective therapy [95]. Although PET is widely used for cerebral MRO_2 estimation in adults, the need of ionized radiation prevents it from pediatric population. MRI and NIRS have been applied in neonates, but none of them measures all of the parameters (based on Fick's law). By adopting infrared light and diagnostic-frequency transducers, combined photoacoustic and Doppler ultrasound technique could fulfill all the measurements non-invasively for cerebral MRO_2 estimation in neonatal monitoring, with low-cost, easy setup and more flexibility.

Another possible application is to monitor tissue perfusion and system oxygen consumption through cardiac output and pulmonary artery oxygenation (based on Fick's law), which is important during congenital heart surgery, or for high-risk critically ill surgical patients [96]. Currently pulmonary artery catheter (PAC) is still considered as gold standard method to measure pulmonary artery oxygenation, however, its use has been associated with various complications like pneumothorax, infection, pulmonary artery rupture and valve injury. Since Esophageal Doppler (ED) and trans-esophageal echocardiography (TEE) have been used to monitor cardiac output, it is possible to use combined photoacoustic and Doppler ultrasound endoscope via esophageal access to measure both cardiac output and pulmonary artery oxygenation.

Cancer cells often consumes more oxygen than normal cells due to rapid proliferations. MRO_2 is an important indicator of the supply of oxygen to the rapidly growing tumor, and oxygen

deficiency (hypoxia) is a common feature in tumor cell metastasis. Combined photoacoustic and Doppler ultrasound technique can be used to estimate MRO_2 within a certain tumor region, by imaging oxygenation levels and flow rates of the feeding and draining vessels, to help to improve cancer screening, cancer diagnosis, and therapy response monitoring.

To conclude, combined photoacoustic and Doppler ultrasound technique has strong potential for the study of metabolism in brain, cancer, tissue perfusion monitoring, and other metabolic related diseases, treatment and applications.

Bibliography

[1] H. F. Zhang, K. Maslov, G. Stoica, L. V. Wang, "Functional photoacoustic microscopy for high-resolution and noninvasive *in vivo* imaging," *Nature Biotechnology,* vol. 24, pp. 848-851 , 2006.

[2] T. N. Seyfried, L. M. Shelton, "Cancer as a metabolic disease," *Nutrition and Metabolism,* vol. 7, no. 7, pp. 1-22, 2010.

[3] P. Vaupel, F. Kallinowski, P. Okunieff, "Blood flow, oxygen and nutrient supply, and metabolic microenvironment of human tumors: a review," *Cancer Research,* vol. 49, no. 23, pp. 6449-6465, 1989.

[4] A. Zhu, D. Lee, H. Shim, "Metabolic PET imaging in cancer detection and therapy response," *Seminers in Oncology,* vol. 38, no. 1, pp. 55-69, 2012.

[5] R. J. Person, R. Thies, Physiology 2nd Edition, New York: Springer-Verlag New York Inc., 1989.

[6] K. Ishii, H. Kitagaki, M. Kono, E. Mori, "Decreased medical temporal oxygen metabolism in Alzheimer's disease shown by PET," *Jounal of Nuclear Medicine,* vol. 37, no. 7, pp. 1159-1165, 1996.

[7] R. F. Peppard, W. R. Wayne Martin, G. D. Carr, et al., "Cerebral glucose metabolism in Parkinson's disease with and without dementia," *Archives of Neurology,* vol. 49, no. 12, pp. 1262-1268, 1992.

[8] P. Santens, J. De Reuck, L. Crevits, D. Decoo, I. Lemahieu, K. Strijckmans, P. Goethals, "Cerebral oxygen metabolism in patients with progressive supranuclear palsy: a positron emission tomography study," *European Neurology,* vol. 37, no. 1, pp. 18-22, 1997.

[9] P. Maquet, "Sleep functions and cerebral metabolism," *Behavioural Brain Research,* vol. 69, no. 1-2, pp. 75-83, 1995.

[10] V. Bonhomme, PBoverous, P. Hans, J. F. Brichant, A. Vanhaudenhuyse, M. Boly, S. Laureys, "Influence of anesthesia on cerebral blood flow, cerebral metabolic rate, and brain functional connectivity," *Anesthesiology,* vol. 24, no. 5, pp. 474-479, 2011.

[11] G. Marchal, P. Rioux, M. C. Petit-Taboue, G. Sette, J. M. Travere, C. LePoec, P. Courtheoux, J. M. Derlon, J. C. Baron, "Regional cerebral oxygen consumption, blood flow, and blood volume in healthy human aging," *Archives of Neurology,* vol. 49, no. 10, pp. 1013-1020, 1992.

[12] J. B. De Vis, E. T. Petersen, A. Bhogal, N. S. Hartkamp, C. J. M. Klijin, L. J. Kappelle, J. Hendrikse, "Calibrated MRI to evaluate cerebral hemodynamics in patients with an internal carotid artery occlusion," *Journal of Cerebral Blood Flow and Metabolism,* vol. 35, no. 6, pp. 1015-1023, 2015.

[13] I. R. Sweet, G. Khalil, A. R. Wallen, M. Steedman, K. A. Schenkman, J. A. Reems, S. E. Kahn, "Continuous measurement of oxygen consumption by pancreatic islets," *Diabetes Technology and Therapeutics,* vol. 4, no. 5, pp. 661-672, 2004.

[14] T. Tadros, D. L. Traber, D. N. Herndon, "Hepatic blood flow and oxygen consumption after burn and sepsis," *The Journal of Trauma: Injury, Infection, and Critical Care,* vol. 49, no. 1, pp. 101-108, 2000.

[15] J. B. De Vis, E. T. Petersen, A. Bhogal, N. S. Hartkamp, C. J. M. Klijin, L. J. Kappelle, J. Hendrikse, "Calibrated MRI to evaluate cerebral hemodynamics in patients with an internal carotid artery occlusion," *Journal of Cerebral Blood Flow and Metabolism,* vol. 35, no. 6, pp. 1015-1023, 2015.

[16] R. M. Bersin, C. Wolfe, M. Kwasman, et. al. , "Improved hemofynamic function and mechanical efficiency in congestive heart failure with sodium dichloroacretate," *Journal of the American College of Cardiology,* vol. 23, no. 7, pp. 1617-1624, 1994.

[17] L. V. Wang, "Prospects of photoacoustic tomography," *Medical Physics,* vol. 35, no. 12, pp. 5758-5767, 2008.

[18] T. Christen, D. S. bolar, G. Zaharchuk, "Imaging brain oxygenation with MRI using oxygenation approaches: methods, validation, and clinical applications," *American Journal of Neuroradiology,* vol. 34, no. 6, pp. 1113-1123, 2013.

[19] T. S. Mayberg, A. M. Lam, "Jugular bulb oximetry for the monitoring of cerebral blood flow and metabolism," *Neurosurgery Clinics of North America,* vol. 7, no. 4, pp. 755-765 , 1996.

[20] Y. Yamamoto, R. de Silva, C. G. Rhodes, H. Iida, A. A. Lammertsma, T. Jones, A. Maseri, "Noninvasive quantification of regional myocardial metabolic rate of oxygen by 15O2 inhalation and positron emission tomography," *Circulation,* vol. 94, pp. 808-816, 1996.

[21] E. M. Haacke, S. Lai, J. R. Reichenbach, K. Kuppusamy, F. G. C. Hoogenraad, H. Takeichi, and W. L. Lin, "*In vivo* measurement of blood oxygen saturation using magnetic resonance imaging: A direct validation of the blood oxygen level-dependent concept in functional brain imaging," *Human Brain Mapping,* vol. 5, pp. 341-346, 1997.

[22] G. Yu, T. Durduran, G. Lech, C. Zhou, B. Chance, E. R. Mohler, A. G. Yodh, "Time-dependent blood flow and oxygenation in human skeletal muscles measured with noninvasive near-infrared diffuse optical spectroscopies," *Journal of Biomedical Optics,* vol. 10, no. 2, p. 024027, 2005.

[23] L. A. Steiner, D. Pfister, S. P. Strebel, D. Radolovich, P. Smielewski, "Near-Infrared Spectroscopy can monitor dynamic cerebral autoregulation in adults," *Neurocritical Care Society,* vol. 10, no. 1, pp. 122-128, 2009.

[24] J. Yao, K. Maslov, Y. Zhang, Y. Xia, L. V. Wang, "Label-free oxygen-metabolic photoacoustic microscopy *in vivo*," *Journal of Biomedical Optics,* vol. 16, no. 7, p. 076003, 2011.

[25] J. Yao, L. V. Wang, "Transverse flow imaging based on photoacoustic Doppler bandwidth broadening," *Journal of Biomedical Optics,* vol. 15, no. 2, p. 021304, 2010.

[26] J. Brunker, P. Beard, "Velocity measurements in whole blood using acoustic resolution photoacoustic Doppler," *Biomedical Optics Express,* vol. 7, no. 7, pp. 2789-2806, 2016.

[27] C. Kasai, K. Namekawa, A. Koyano, and R. Omoto, "Real-time two-dimensional blood flow imaging using an autocorrelation technique," *IEEE Transactions on sonics and ultrasonics ,* vol. 32, p. 458–463, 1985.

[28] J. M. Brown, W. R. Wilson, "Exploiting tumour hypoxia in cancer treatment," *Nature Reviews Cancer,* vol. 4, no. 6, p. 437–447, 2004.

[29] C. S. Kidwell, J. R. Alger, J. L. Saver, "Beyond mismatch: evolving paradigms in imaging the ischemic penumbra with multimodal magnetic resonance imaging," *Stroke,* vol. 34, no. 11, pp. 2729-2735, 2003.

[30] P. L. Marino, K. M. Sutin, The ICU Book, Philadelphia, USA: Lippincott Williams & Wilkins.

[31] E. M. Rohren, T. G. Turkington, R. E. Coleman, "Clinical applications of PET in oncology," *Radiology,* vol. 231, no. 2, pp. 305-332, 2004.

[32] H. Ito, M. Ibaraki, I. Kanno, H. Fukuda, S. Miura, "Changes in cerebral blood flow and cerebral oxygen metabolism during neural activation measured by positron emission tomography: comparison with blood oxygenation level-dependent contrast measured by functional magnetic resonance imaging," *Journal of Cerebral Blood Flow and Metabolism,* vol. 25, no. 3, pp. 371-377, 2005.

[33] G. H. Glover, "Overview of functional magnetic resonance imaging," *Neurosurgery Clinics of North America,* vol. 22, no. 2, p. 133–139, 2011.

[34] F. Xu, Y. Ge, H. Lu, "Noninvasive quantification of whole-brain cerebral metabolic rate of oxygen ($CMRO_2$) by MRI," *Magnetic Resonance in Medicine,* vol. 62, no. 1, pp. 141-148, 2009.

[35] V. Jain, M. C. Langham, F. W. Wehrli, "MRI estimation of global brain oxygen consumption rate," *Journal of Cerebral Blood Flow and Metabolism,* vol. 30, no. 9, pp. 1598-1607, 2010.

[36] M. Ghijsen, G. R. Lentsch, S. Gioux, M. Brenner, A. J. Durkin, B. Choi, B. J. Tromberg, "Quantitative real-time optical imaging of the tissue metabolic rate of oxygen consumption," *Journal of Biomedical Optics,* vol. 23, no. 3, p. 036013, 2018.

[37] K. J. Taylor, P. Burns, P. Wells, Clinical Applications of Doppler Ultrasound, New York: Lippincott-Raven, 1995.

[38] R. S. C. Cobbold, Foundations of Biomedical Ultrasound, New York: Oxford University Press, 2007.

[39] J. M. J. G. Roevros, Cardiovascular Applications of Ultrasound, Amsterdam: North-Holland Publication, 1974.

[40] W. R. Brody, "Theoretical analysis of the CW ultrasonic flowmeter," *IEEE Transaction of Biomedical Engineering,* vol. 43, pp. 562-571, 1996.

[41] J. A. Jenson, Estimation of Blood Velocities Using Ultrasound: A Signal Processing Approach, Cambridge: Cambridge University Press, 1996.

[42] P. S. Green, "Spectral broadening of acoustic reverberation in Doppler-shift fluid flowmetries," *Journal of the Acoustic Society of America,* vol. 36, pp. 1383-1390 , 1964.

[43] G. Guidi, C. Licciardello, S. Falteri, "Intrinsic spectral broadening (ISB) in ultrasound Doppler as a combination of transit time and local geometrical broadening," *Ultrasound in Medicine and Biology,* vol. 26, no. 5, pp. 853-862, 2000.

[44] O. W. Ata, P. J. Fish, "Effect of deviation from plane wave conditions on the Doppler spectrum from an ultrasonic blood flow detector," *Ultrasonics ,* vol. 29, no. 5, pp. 395-403, 1991.

[45] D. Censor, V. L. Newhouse, T. Vontz, H. V. Ortega, "Theory of ultrasound Dopper-spectra velocimetry for arbitrary beam and flow configurations," *IEEE Transaction of Biomedical Engineering,* vol. 35, no. 9, pp. 740-751, 1988.

[46] P. N. Burns, "The physical principles of Doppler and spectral analysis," *Journal of Clinical Ultrasound,* vol. 15, pp. 567-590, 1987.

[47] N. S. Anavekar, J. K. Oh, "Doppler echocardiography: a contemporary review," *Journal of Cardiology,* vol. 54, no. 3, pp. 347-358, 2009.

[48] O. Bonnefous, P. Pesqué, "Time domain formulation of pulse-Doppler ultrasound and blood velocity estimation by cross correlation," *Ultrasonic Imaging,* vol. 8, no. 2, pp. 73-85, 1986.

[49] D. H. Evans, J. A. Jensen, M. B. Nielsen, "Ultrasonic colour Doppler imaging," *Interface Focus (2011) 1, S,* vol. 1, p. 490–502, 2011.

[50] A. J. Bjorn, "Instantaneous frequency, mean frequency, and variance of mean frequency estimators for ultrasonic blood velocity Doppler signals," *IEEE Transaction on Biomedical Engineering,* vol. 28, no. 11, pp. 733-741 , 1981.

[51] B. Lee, H. K. Chiang, C. Kuo, W. Lin, S. Lee, "Doppler angle and flow velocity estimations using the classic and transverse Doppler effects," *IEEE Transactions on Ultrasonics, Ferroelectronics,* vol. 46, no. 1, pp. 252-256, 1999.

[52] J. M. Rubin, R. O. Bude, P. L. Carson, R. L. Bree, R. S. Adler, "Power Doppler US: a potentially useful alternative to mean frequency-based color Doppler US," *Radiology,* vol. 190, no. 3, pp. 853-856, 1996.

[53] J. Folkman, "Angiogenesis: an organizing principle for drug discovery?," *Nature Reviews Drug Discovery ,* vol. 6, no. 4, pp. 273-286 , 2007.

[54] J. A. Jenson, "Stationary echo canceling in velocity estimation by time-domain cross-correlation," *IEEE Transactions on Medical Imaging,* vol. 12, no. 3, pp. 471 - 477, 1993.

[55] A. Heimdal, H. Torp, "Ultrasound doppler measurements of low velocity blood flow: limitations due to clutter signals from vibrating muscles," *IEEE Transactions on Ultrasonics, Ferroelectrics, and Frequency Control,* vol. 44, no. 4, pp. 873 - 881, 1997.

[56] D. Kruse, R. Silverman, S. Erickson, D. J. Coleman, K. W. Ferrara, "Optimization of real-time high frequency ultrasound for blood flow imaging in microcirculation," *IEEE Ultrasonics Symposium,* vol. 2, pp. 1461-1464, 2000.

[57] D. E. Kruse, K. W. Ferrara, "A new high resolution color flow system using an eigendecomposition-based adaptive filter for clutter rejection," *Ultrasonics, Ferroelectrics and frequency control IEEE Transactions ,* vol. 40, no. 12, pp. 1739-1753 , 2002.

[58] D. G. Manolakis, D. Manolakis, V. K. Ingle, S. M. Kogon, Statistical and Adaptive Signal Processing: Spectral Estimation, Signal Modeling, Adaptive Filtering and Array Processing, Boston, MA: McGraw-Hill, 2000.

[59] M. Xu, L. V. Wang, "Photoacoustic imaging in biomedicine," *Review of Scientific Instruments,* vol. 77, p. 041101, 2006.

[60] L. V. Wang, "Tutorial on photoacoustic microscopy and computed tomography," *IEEE Journal of Selected Topics in Quantum Electronics,* vol. 14, no. 1, pp. 171-179, 2008.

[61] A. A. Oraevsky, A. A. Karabutov, Biomedical Photonics Handbook, Boca Raton, FL: CRC, 2003.

[62] L. V. Wang, H. Wu, Biomedical Optics: Principles and Imaging, Hoboken, New Jersey: John Wiley & Sons, Inc., 2007.

[63] H. F. Zhang, K. Maslov, M. Sivaramakrishnan, "Imaging of hemoglobin oxygen saturation variations in single vessels *in vivo* using photoacoustic microscopy," *Applied Physics Letters,* vol. 90, p. 053901, 2007.

[64] X. Wang, Y. Pang, G. Ku, X. Xie, G. Stoica, L. V. Wang, "Noninvasive laser-induced photoacoustic tomography for structural and functional *in vivo* imaging of the brain," *Nature Biotechnology,* vol. 21, pp. 803-806, 2003.

[65] J. Yao, L. V. Wang, "Photoacoustic tomography fundamentals,advances and prospects," *Contrast Media & Molecular Imaging.,* vol. 6, p. 332–345 , 2011.

[66] J. Yao, L. V. Wang, "Photoacoustic microscopy," *Laser & Photonics Reviews,* vol. 7, no. 5, pp. 758-778, 2013.

[67] K. Maslov, H. Zhang, S. Hu, L. V. Wang, "Optical-resolution photoacoustic microscopy for *in vivo* imaging of single capillaries," *Optics Letters ,* vol. 33, no. 9, pp. 929-931, 2008.

[68] K. Maslov, G. Stoica, L. V. Wang, "*In vivo* dark-field reflection-mode photoacoustic microscopy," *Optics Letters,* vol. 30, p. 625–627, 2005.

[69] S. Hu, K. Maslov, L. V. Wang, "Noninvasive label-free imaging of microhemodynamics by optical-resolution photoacoustic microscopy," *Optics Express,* vol. 17, p. 7688–7693, 2009.

[70] J. Xia, A. Danielli, Y. Liu, L. Wang, K. Maslov, L. V. Wang, "Calibration-free quantification of absolute oxygen saturation based on the dynamics of photoacoustic signals," *Optics Letters,* vol. 38, no. 15, pp. 2800-2803, 2013.

[71] J. A. Ketterling, O. Aristiz´abal, D. H. Turnbull, F. L. Lizzi, "Design and fabrication of a 40MHz annular array transducer," *Ultrasonics, Ferroelectrics and Frequency Control, IEEE Transactions,* vol. 52, no. 4, pp. 672-681 , 2005.

[72] S. Z. Pinter, J. C. Lacefield, "Detectability of small blood vessels with high-frequency power Doppler and selection of wall filter cut-off velocity for microvascular imaging," *Ultrasound in Medicine and Biology,* vol. 35, no. 7, pp. 1217-1228, 2009.

[73] R. J. Zemp, C. Kim, L. V. Wang, "Ultrasound-modulated optical tomography with intense acoustic bursts," *Applied Optics,* vol. 46, no. 10, pp. 1615-1623, 2007.

[74] B. G. Zagar, R. J. Fornaris, K. W. Ferrara, "Ultrasonic mapping of the microvasculature: signal alignment," *Ultrasound in Medicine and Biology,* vol. 24, no. 6, pp. 809-824, 1998.

[75] A. Needle, D. E. Goertz, A. M. Cheung, F. S. Foster, "Inter-frame clutter filtering for high frequency flow imaging," *Ultrasound in Medicine and Biology,* vol. 33, no. 4, pp. 591-600, 2007.

[76] P. Horstmann, "The oxygen consumption in diabetes mellitus," *1951,* vol. 139, no. 4, pp. 326-330, Acta Medica Scandinavica .

[77] T. Liu, Q. Wei, J. Wang, S. Jiao, H. F. Zhang, "Combined photoacoustic microscopy and optical coherence tomography can measure metabolic rate of oxygen," *Biomedical Optics Express ,* vol. 2, no. 5, pp. 1359-1365, 2011.

[78] Y. Jiang, T. Harrison, J. C. Ranasinghesagara, R. J. Zemp, "Photoacoustic and high-frequency power Doppler ultrasound biomicroscopy: a comparative study," *Journal of Biomedical Optics,* vol. 15, no. 5, p. 056008, 2010.

[79] T. Harrison, J. C. Ranasinghesagara, H. H. Lu, K. Mathewson, A. Walsh, R. J. Zemp, "Combined photoacoustic and ultrasound biomicroscopy," *Optics Express,* vol. 17, no. 24, pp. 22041-22046, 2009.

[80] Y. Jiang, T. Harrison, A. Forbrich, R. J. Zemp, "Oxygen consumption estimation with combined color Doppler ultrasound and photoacoustic microscopy: a phantom study," *Proc. SPIE 7899,* p. 789942 , 2011.

[81] G. R. Kelman, "Digital computer subroutine of the conversion of oxygen tension into saturation," *Journal of Applied Physiology,* vol. 21, no. 4, pp. 1375-1376, 1966.

[82] D. E. Ullrey, E. R. Miller, C. H. Long, B. H. Vincent, "Sheep hematology from birth to maturity I. erythrocyte population, size and hemoglobin concentration," *Journal of Animal Science ,* vol. 24, no. 1, pp. 135-140 , 1965.

[83] R. C. Tasker, "Brain vascular and hydrodynamic physiology," *Semin. Pediatr. Surg. ,* vol. 22, no. 4, pp. 168-173, 2013.

[84] A. A. Scand, "Regional cerebral blood flow and glucose metabolism during propofol anesthesia in healthy subjects studied with positron emission tomography," *Acta Anaesthesiol. Scandinavica ,* vol. 56, no. 2, pp. 248-255 , 2012.

[85] M. N. Diringer, V. Aiyagari, A. R. Zazulia, T. O. Videen, W. J. Powers, "Effect of hyperoxia on cerebral metabolic rate for oxygen measured using positron emission tomography in patients with acute severe head injury," *J. Neurosurg.,* vol. 106, no. 4, pp. 526-529 .

[86] S. S. Kety, C. f. Schmidt, "The effect of altered arterial tensions of carbon dioxide and oxygen on cerebral blood flow and cerebral oxygen consumption of normal young men," *J. Clin. Invest.,* vol. 27, no. 4, pp. 484-492, 1948.

[87] S. P. Chong, C. W. Merkle, C. Leahy, V. J. Srinivasan, "Cerebral metabolic rate of oxygen ($CMRO_2$) assessed by combined Doppler and spectroscopic OCT," *Biomed. Opt. Express,* vol. 6, no. 10, pp. 3941-3951 , 2015.

[88] F. Xu, P. Liu, J. M. Pascual, G. Xiao, H. Lu, "Effect of hypoxia and hyperoxia on cerebral blood flow, blood oxygenation, and oxidative metabolism," *Journal of Cerebral Blood Flow & Metabolism ,* vol. 32, no. 10, pp. 1909-1918, 2012.

[89] M. J. Cipolla, The Cerebral Circulation, Morgan & Claypool Life Sciences, 2009.

[90] Y. Jiang, A. Forbrich, T. Harrison, R. J. Zemp, "Blood oxygen flux estimation with a combined photoacoustic and high-frequency ultrasound microscopy system: a phantom study," *Journal of Biomedical Optics ,* vol. 17, no. 3, p. 036012, 2012.

[91] J. B. West, Pulmonary physiology and pathophysiology: an integrated, case-based approach. 2nd ed., Philadelphia, PA: Lippincott Williams & Wilkins.

[92] H. Ohsumi, K. Kitaquchi, T. Nakajima, Y. Ohnishi, M. Kuro, "Internal jugular bulb blood velocity as a continuous indicator of cerebral blood flow during open heart surgery," *Anesthesiology,* vol. 81, no. 2, pp. 325-332, 1994.

[93] Shung, K Kirk, "High frequency ultrasonic imaging," *Journal of Medical Ultrasound ,* vol. 17, no. 1, pp. 25-30, 2009.

[94] Bauer AQ, Nothdurft RE, Erpelding TN, Wang LV, Culver JP., "Quantitative photoacoustic imaging: correcting for heterogeneous light fluence distributions using diffuse optical tomography," *Journal of Biomedical Optics,* vol. 16, no. 9, p. 096016, 2011.

[95] P. Liu, L. F. Chalak, H. Lu, "Non-invasive assessment of neonatal brain oxygen metabolism: a review of newly available techniques," *Early Human Development,* vol. 90, no. 10, pp. 695-701, 2014.

[96] Y. Mehta, D. Arora, "Newer methods of cardiac output monitoring," *World Journal of Cardiology,* vol. 6, no. 9, pp. 1022-1029, 2014.